Production of HONO from NO_2 uptake on illuminated TiO_2 aerosol particles and following the illumination of mixed TiO_2/ammonium nitrate particles.

Joanna E. Dyson[1], Graham A. Boustead[1], Lauren T. Fleming[1], Mark Blitz[1, 2], Daniel Stone[1], Stephen R. Arnold[3], Lisa K. Whalley[1, 2], Dwayne E. Heard[1]*

[1] School of Chemistry, University of Leeds, LS2 9JT, UK.

[2] National Centre of Atmospheric Science, University of Leeds, LS2 9JT, UK.

[3] School of Earth and Environment, University of Leeds, LS2 9JT, UK.

*Corresponding Author. Email: D.E.Heard@leeds.ac.uk

Abstract

The rate of production of HONO from illuminated TiO_2 aerosols in the presence of NO_2 was measured using an aerosol flow tube system coupled to a photo-fragmentation laser induced fluorescence detection apparatus. The reactive uptake coefficient of NO_2 to form HONO, $\gamma_{NO_2 \rightarrow HONO}$, was determined for NO_2 mixing ratios in the range $34 - 400$ ppb, with $\gamma_{NO_2 \rightarrow HONO}$ spanning the range $(9.97 \pm 3.52) \times 10^{-6}$ to $(1.26 \pm 0.17) \times 10^{-4}$ at a relative humidity of 15 ± 1 % and for a lamp photon flux of $(1.63 \pm 0.09) \times 10^{16}$ photons cm^{-2} s^{-1} (integrated between 290 and 400 nm), which is similar to midday ambient actinic flux values. $\gamma_{NO_2 \rightarrow HONO}$ increased as a function of NO_2 mixing ratio at low NO_2 before peaking at $(1.26 \pm 0.17) \times 10^{-4}$ at ~51 ppb NO_2 and then sharply decreasing at higher NO_2 mixing ratios, rather than levelling off which would be indicative of surface saturation. The dependence of HONO production on relative humidity was also investigated, with a peak in production of HONO from TiO_2 aerosol surfaces found at ~25 % RH. Possible mechanisms consistent with the observed trends in both the HONO production and reactive uptake coefficient were investigated using a zero-dimensional kinetic box model. The modelling studies supported a mechanism for HONO production on the aerosol surface involving two molecules of NO_2, as well as a surface HONO loss mechanism which is dependent upon NO_2. In a separate experiment, significant production of HONO was observed from illumination of mixed nitrate/TiO_2 aerosols in the absence of NO_2. However, no production of HONO was seen from the illumination of nitrate aerosols alone. The rate of production of HONO observed from mixed nitrate/TiO_2 aerosols was scaled to ambient conditions found at the Cape Verde Atmospheric Observatory (CVAO) in the remote

tropical marine boundary layer. The rate of HONO production from aerosol particulate nitrate photolysis containing a photocatalyst was found to be similar to the missing HONO production rate necessary to reproduce observed concentrations of HONO at CVAO. These results provide evidence that particulate nitrate photolysis may have a significant impact on the production of HONO and hence NO_x in the marine boundary layer where mixed aerosols containing nitrate and a photocatalytic species such as TiO_2, as found in dust, are present.

1 Introduction

A dominant source of OH radicals in polluted environments is the photolysis of nitrous acid (HONO) (Platt et al., 1980;Winer and Biermann, 1994;Harrison et al., 1996;Alicke et al., 2002;Whalley et al., 2018;Crilley et al., 2019;Lu et al., 2019;Slater et al., 2020;Whalley et al., 2020). During a recent study in Winter in central Beijing, HONO photolysis accounted for over 90 % of the primary production of OH averaged over the day (Slater et al., 2020). Oxidation by OH radicals is the dominant removal mechanism for many tropospheric trace gases, such as tropospheric methane, as well as the formation of secondary species, including tropospheric ozone (Levy, 1971), nitric and sulphuric acids which condense to form aerosols, and secondary organic aerosols. Understanding the formation of HONO in highly polluted environments is crucial to fully understand both the concentration and distribution of key atmospheric radical species, as well as secondary products in the gas and aerosol phases associated with climate change and poor air quality.

Atmospheric concentrations of HONO range from a few pptv in remote clean environments (Reed et al., 2017) to more than 10 ppb in highly polluted areas such as Beijing (Crilley et al., 2019). The main gas-phase source of HONO in the troposphere is the reaction of nitric oxide (NO) with the OH radical. HONO has also been shown to be directly emitted from vehicles (Kurtenbach et al., 2001;Li et al., 2008), for which the rate of emission is often estimated as a fraction of known NO_x (NO_2+NO) emissions. Many heterogeneous HONO sources have also been postulated including the conversion of nitric acid (HNO_3) on ground or canopy surfaces (Zhou et al., 2003;George et al., 2005), bacterial production of nitrite on soil surfaces (Su et al., 2011;Oswald et al., 2013) and, more recently, particulate nitrate photolysis, thought to be an important source in marine environments (Ye et al., 2016;Reed et al., 2017;Ye et al., 2017a;Ye et al., 2017b). Rapid cycling of gas-phase nitric acid to gas-phase nitrous acid via particulate nitrate photolysis in the clean marine boundary layer has been observed during the

63   2013 NOMADSS aircraft measurements campaign over the North Atlantic Ocean (Ye et al.,

64   2016). Ground-based measurements of HONO made at Cape Verde in the tropical Atlantic

65   Ocean (Reed et al., 2017) provided evidence that a mechanism for renoxification in low NO_x

66   areas is required (Reed et al., 2017;Ye et al., 2017a).
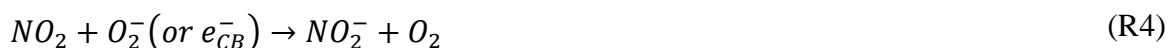
67   Recent model calculations show a missing daytime source of HONO, which is not consistent

68   with known gas-phase production mechanisms, direct emissions or dark heterogeneous

69   formation (e.g. prevalent at night). It has been suggested that this source could be light driven

70   and dependent on NO_2 (Kleffmann, 2007;Michoud et al., 2014;Spataro and Ianniello, 2014;Lee

71   et al., 2016).

72   It is estimated that between 1604 and 1960 Tg yr^{-1} of dust particles are emitted into the

73   atmosphere (Ginoux et al., 2001). Titanium dioxide (TiO_2) is a photocatalytic compound found

74   in dust particles at mass mixing ratios of between 0.1 and 10 % depending on the location the

75   particles were suspended (Hanisch and Crowley, 2003). When exposed to UV light ($\lambda < 390$

76   nm) TiO_2 promotes an electron (e_{CB}^-) from the conduction band to the valence band leaving

77   behind a positively charged hole (h_{VB}^+) in the valence band (Chen et al., 2012):

$$TiO_2 + h\nu \rightarrow e_{CB}^- + h_{VB}^+ \tag{R1}$$

78   which can then lead to both reduction and oxidation reactions of any surface adsorbed gas-

79   phase species such as NO_2 leading to HONO.

80   In previous studies of the reaction of NO_2 on TiO_2 aerosol surfaces, HONO was observed as a

81   major gas-phase product (Gustafsson et al., 2006;Dupart et al., 2014). Gustafsson *et al.*, (2006)

82   observed a yield of gas-phase HONO of ~ 75 % (for each NO_2 removed), and showed the rate

83   of the photoreaction of NO_2 on pure TiO_2 aerosols depended on relative humidity, emphasising

84   the superhydrophilic nature of TiO_2 surfaces under UV irradiation. Dupart *et al.* (2014) also

85   reported a relative humidity dependence of the uptake of NO_2 onto Arizona Test Dust

86   containing TiO_2 with the main gas-phase products measured being NO and HONO, with a

87   HONO yield of 30 % in experiments with 110 ppb NO_2. Dupart et al. (2014) postulated the

88   following mechanism of HONO production, which is consistent with the formation of the NO_2^-

89   anion seen in a previous study on TiO_2 surfaces (Nakamura et al., 2000):

$$h_{VB}^+ + H_2O \rightarrow H^+ + OH \tag{R2}$$

$$e_{CB}^- + O_2 \rightarrow O_2^- \tag{R3}$$

$$NO_2 + O_2^- \left(or\ e_{CB}^- \right) \rightarrow NO_2^- + O_2 \tag{R4}$$

$$NO_2^- + H^+ \rightarrow HONO \tag{R5}$$

$$NO_2 + OH \rightarrow HNO_3 \tag{R6}$$

In areas with high mineral dust loading, such as desert regions, far from anthropogenic sources, NO_2 concentrations are typically low. However, when dust is transported to urban areas, this source of HONO may become significant. One study reported that TiO_2 composed 0.75-1.58 $\mu g\ m^{-3}$ when aerosol loadings were 250-520 $\mu g\ m^{-3}$ over the same time period in southeast Beijing, when air had been transported from the Gobi desert (Schleicher et al., 2010).

In this study, the production of HONO on the surface of TiO_2 particles in the presence of NO_2 is investigated as a function of NO_2 mixing ratio, aerosol surface area density and relative humidity using an aerosol flow tube system coupled to a photo-fragmentation laser induced fluorescence detector (Boustead, 2019). The uptake coefficient of NO_2 to generate HONO is then determined, and a mechanistic interpretation of the experimental observations is presented. The production of HONO directly in the absence of NO_2 from the illumination of a mixed sample of nitrate and TiO_2 aerosol is also presented. Using a similar apparatus, previous work had showed that TiO_2 particles produce OH and HO_2 radicals directly under UV illumination (Moon et al., 2019). The atmospheric implications of these results and the role of photo-catalysts for the formation of HONO are also discussed.

2 Method

2.1 Overview of the Experimental Setup

The production of HONO from illuminated aerosol surfaces is studied using an aerosol flow tube system coupled to a photo-fragmentation laser induced fluorescence (PF-LIF) cell which allows the highly sensitive detection of the OH radical formed through photo-fragmentation of HONO into OH and NO followed by Laser-Induced Fluorescence (LIF) detection at low pressure. The experimental setup used in this investigation is described in detail in (Boustead, 2019), as well as similar systems having been used to measure HONO in the field (Liao et al., 2006;Wang et al., 2020),and therefore only a brief description of the setup is given here. A schematic of the experimental setup is shown in Figure 1.
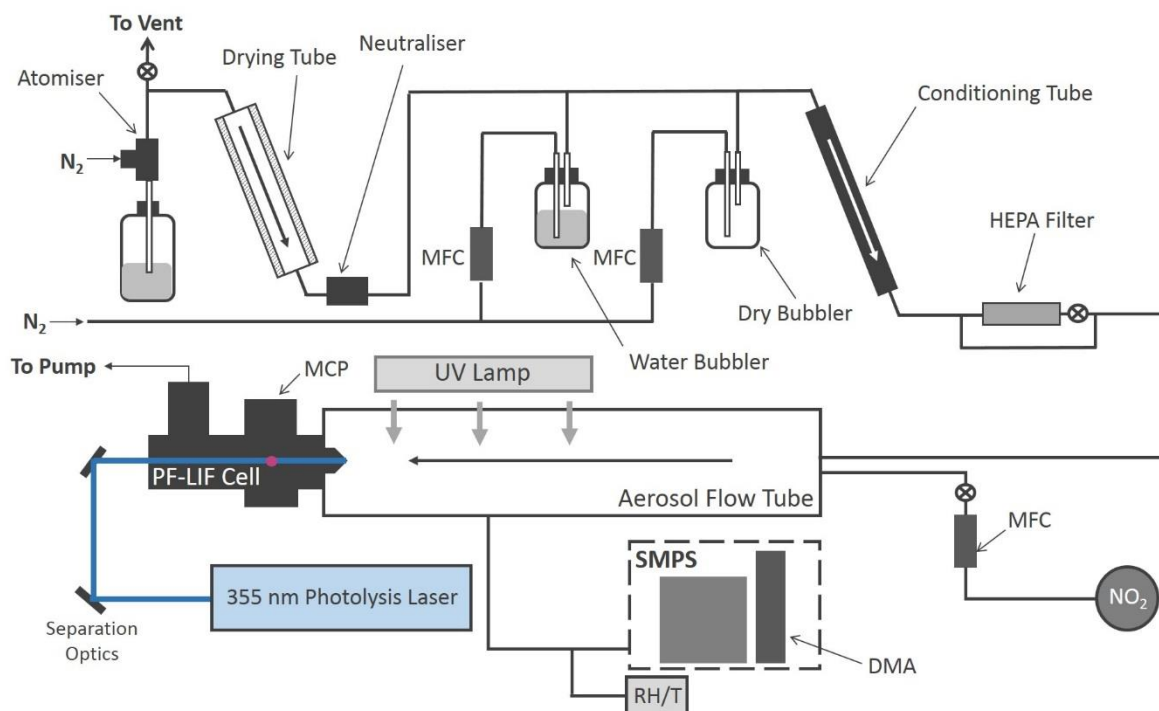
Figure 1. Schematic of the Leeds aerosol flow tube system coupled to a laser-fragmentation laser-induced fluorescence detector for HONO. The paths of the 355 nm (blue) and 308 nm (purple, depicted as travelling out of the page perpendicular to the 355 nm light) light are also shown. CPC: condensation particle counter; DMA: differential mobility analyser; HEPA: high efficiency particle air filter; FAGE: fluorescence assay by gas expansion; MCP: microchannel plate photomultiplier; MFC: mass flow controller; RH/T: relative humidity/ temperature probe; SMPS: scanning mobility particle sizer.

115

116   All experiments were conducted at room temperature (295 ± 3 K) using nitrogen (BOC, 99.998
117   %) or air (BOC, 21 ± 0.5 % O_2) as the carrier gas. A humidified flow of aerosols, ~ 6 lpm (total
118   residence time of 104 s in the flow tube), was introduced through an inlet at the rear of the
119   aerosol flow tube (Quartz, 100 cm long, 11.5 cm ID) which was covered by a black box to
120   eliminate the presence of room light during experiments. A 15 W UV lamp (XX-15LW Bench
121   Lamp, λ_{peak}=365 nm) was situated on the outside of the flow tube to illuminate aerosols and
122   promote the production of HONO (half the length of the flow tube was illuminated leading to
123   an illumination time of 52 s). The concentration of HONO is measured by PF-LIF with
124   sampling from the end of the flow tube via a protruding turret containing a 1 mm diameter
125   pinhole, through which the gas exiting the flow tube was drawn into the detection cell at 5 lpm.
126   The detection cell was kept at low pressure, ~ 1.5 Torr, using a rotary pump (Edwards, E1M80)
127   in combination with a roots blower (Edwards, EH1200). All gas flows in the experiment were
128   controlled using mass flow controllers (MKS and Brooks). The relative humidity (RH) and
129   temperature of the aerosol flow was measured using a probe (Rotronics HC2-S, accuracy ±1

130　% RH) the former calibrated against the H_2O vapour concentration measured by a chilled

131　mirror hygrometer (General Eastern Optica), in the exhaust from the flow tube.

2.2　Aerosol generation and detection

133　Solutions for the generation of TiO_2 aerosol solutions were prepared by dissolving 5 g of

134　titanium dioxide (Aldrich Chemistry 718467, 99.5% Degussa, 80 % anatase: 20 % rutile) into

135　500 ml of milli-Q water. Polydisperse aerosols were then generated from this solution using an

136　atomiser (TSI model 3076) creating a 1 lpm flow of TiO_2 aerosol particles in nitrogen hereafter

137　referred to as the aerosol flow. This aerosol flow was then passed through a silica drying tube

138　(TSI 3062, capable of reducing 60 % RH incoming flow to 20 % RH) to remove water vapour,

139　then passed through a neutraliser to apply a known charge distribution and reduce loss of

140　aerosols to the walls. After the neutraliser the aerosol flow was mixed with both a dry and a

141　humidified N_2 flow (controlled by MFCs) to regulate the relative humidity of the system by

142　changing the ratio of dry to humid nitrogen flows. A conditioning tube was then used to allow

143　for equilibration of water vapour adsorption and re-evaporation to and from the aerosol surfaces

144　for the chosen RH, which was controlled within the range ~10-70 % RH. A portion of the

145　aerosol flow was then passed through a high efficiency particle filter (HEPA) fitted with a

146　bypass loop and bellows valve allowing control of the aerosol number concentration entering

147　the aerosol flow tube. Previous studies (George et al., 2013;Boustead, 2019) have shown the

148　loss of aerosol to the walls of the flow tube to be negligible. Aerosol size distributions were

149　measured for aerosols exiting the flow tube using a scanning mobility particle sizer (SMPS,

150　TSI 3081) and a condensation particle counter (CPC, TSI 3775) which was calibrated using

151　latex beads. Any aerosol surface area not counted due to the upper diameter range of the

152　combined SMPS/CPC (14.6 – 661.2 nm, sheath flow of 3 lpm, instrumental particle counting

153　error of 10-20 %) was corrected for during analysis by assuming a lognormal distribution,

154　which was verified for TiO_2 aerosols generated in this manner (Matthews et al., 2014).

155　However, the majority of aerosols, >90 %, had diameters in the range that could be directly

156　detected. In addition to the experiments with single-component TiO_2, mixed ammonium

157　nitrate/TiO_2 and single-component ammonium nitrate aerosols were also generated using the

158　atomiser for investigations of HONO production from nitrate aerosols without NO_2 present.

159　An example of an aerosol size distribution from this work for single-component ammonium

160　nitrate aerosols, mixed ammonium nitrate/TiO_2 and single-component TiO_2 aerosols is shown
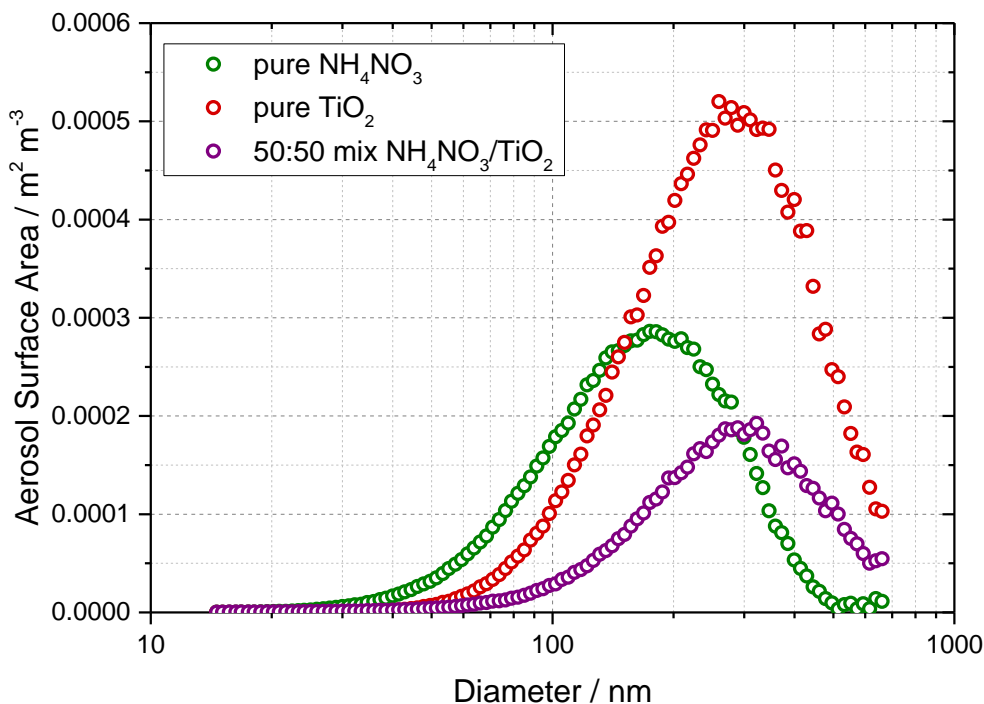
161　in Figure 2.

Figure 2 Typical aerosol surface area distribution for pure ammonium nitrate aerosols (green) and pure TiO$_2$ aerosols (red) and 50:50 mixed nitrate/TiO$_2$ aerosols (purple) measured after the flow tube.

2.3 Detection of HONO

As HONO is not directly detectable via LIF, it was necessary to fragment the HONO produced into OH and NO (Liao et al., 2007), with detection of OH via LIF. A 355 nm photolysis laser (Spectron Laser Systems, SL803) with a pulse repetition frequency (PRF) of 10 Hz and pulse duration ~ 10 ns was used to fragment HONO into OH. This fragmentation wavelength was chosen as HONO has a strong absorption peak at ~ 355 nm leading to the breakage of the HO-NO bond to form NO and OH in their electronic ground states (Shan et al., 1989). A Nd:YAG pumped dye probe laser (JDSU Q201-HD, Q-series, Sirah Cobra Stretch) with a PRF of 5000 Hz, was used for the detection of OH via the fluorescence assay by gas expansion (FAGE) technique which employs the expansion of gas through a small pinhole into the detection cell. The OH radical was measured using on-resonance detection by LIF via the excitation of the $A^2\Sigma^+$ ($v' = 0$) $\leftarrow$ $X\,^2\Pi_i$ ($v'' = 0$) Q$_1$(2) transition at 308 nm (Heard, 2006). A multi-channel plate (MCP) photomultiplier (Photek, MCP 325) equipped with an interference filter at 308 nm (Barr Associates, 308 nm. FWHM – 8 nm, ~50 % transmission) was used to measure the fluorescence signal. A reference OH cell in which a large LIF signal could be generated was utilised to

7

ensure the wavelength of the probe laser remained tuned to the peak of the OH transition at 308 nm. OH measurements are taken both before and after each photolysis laser pulse allowing measurement of any OH already present in the gas flow to be determined as a background signal for subtraction. The OH generated from HONO photolysis was measured promptly (~800 ns) after the 355 nm pulse to maximise sensitivity to OH before it was spatially diluted away from the measurement region (Boustead, 2019). Offline measurements, with the probe laser wavelength moved away from the OH transition (by 0.02 nm), were taken to allow the signal generated from detector dark counts and scattered laser light to be measured and subtracted from the online signal. To determine an absolute value of the HONO concentration, [HONO], a calibration was performed, in order to convert from the HONO signal, S_{HONO}, using $S_{HONO} = C_{HONO}$ [HONO], as described fully in (Boustead, 2019). A glass calibration wand was used to produce OH and HO_2 in equal concentrations from the photolysis of water vapour at 185 nm:

$$H_2O + h\nu \xrightarrow{\lambda=185\ nm} OH + H \tag{R7}$$

$$H + O_2 + M \rightarrow HO_2 + M \tag{R8}$$

An excess flow of NO was then added to generate HONO which was then detected as OH in the cell. The excess flow of NO (BOC, 99.5 %) ensures rapid and complete conversion of OH and HO_2 to HONO. The concentration of OH and HO_2 produced, and therefore the amount of HONO produced in the wand, is calculated using:

$$[OH] = [HO_2] = [H_2O]\ \sigma_{H2O}\ \phi_{OH}\ F\ t \tag{1}$$

where [H_2O] is the concentration of water vapour in the humidified gas flow, σ_{H2O} is the absorption cross section of H_2O at 185 nm (7.14×10^{-20} cm^2 molecule^{-1} (Cantrell et al., 1997), ϕ_{OH} is the quantum yield of OH for the photo-dissociation of H_2O at 185 nm (=1), F is the lamp flux and t is the irradiation time (the product of which is determined using ozone actinometry (Boustead, 2019).

A typical value of the calibration factor was $C_{HONO} = (3.63 \pm 0.51) \times 10^{-9}$ counts mW^{-1} for N_2, leading to a calculated limit of detection of 12 ppt for a 50 s averaging period and a signal-to-noise ratio (SNR) of 1 (Boustead, 2019). The typical error in the HONO concentration was 15% at 1σ, determined by the error in the calibration.

2.4   Experimental procedure and data analysis

The experiments were performed with a minimum flow of 6 lpm through the aerosol flow tube giving a Reynolds number of ~ 150 which ensured a laminar flow regime. The HONO signal, converted to an absolute concentration using a calibration factor, was measured over a range of aerosol surface area densities, both in the presence and absence of illumination, and background measurements without aerosols present, were also performed.

The HONO signal originates from several sources: the illuminated aerosol surface; the illuminated quartz flow tube walls; dark reactions on aerosol surfaces; dark reactions on the flow tube surface and finally from impurities in the NO_2 (Sigma Aldrich, >99.5 %, freeze pump thawed to further remove any remaining NO or O_2) and N_2 flows (either HONO itself or a species which photolyses at 355 nm to give OH). Of interest here is the HONO production from both dark and illuminated aerosol surfaces which is atmospherically relevant. Following transit through the flow tube, and in the presence of NO_2, the total concentration of HONO measured by the PF-LIF detector is given by:

$$[HONO] = [HONO]_{illuminated\ aerosols} + [HONO]_{illuminated\ walls} \\ + [HONO]_{dark\ aerosols} + [HONO]_{dark\ walls} + [HONO]_{impurities}$$

(2)

Any HONO seen without the presence of aerosol was therefore due to HONO impurities in the N_2 or NO_2 gas, the dark production of HONO from the flow tube walls or from the production of HONO from the illuminated reactor walls, which may include production from TiO_2 aerosols coating the flow tube in the presence of NO_2. This background HONO concentration depended on the experimental conditions and on how recently the flow tube and PF-LIF cell had been cleaned to remove any build-up of TiO_2 deposits. However, the build-up of TiO_2 on the flow tube walls was relatively slow and back-to-back measurements were made in the presence and absence of aerosols to obtain an accurate background. Additional experiments showed no significant production of HONO on TiO_2 aerosol surfaces without the presence of NO_2. Even though the aerosol surface area density (~0.02 $m^2\,m^{-3}$) was small compared to the surface area density of the reactor walls (35 $m^2\,m^{-3}$), very little HONO signal was produced without the presence of aerosols, and was always subtracted from the signal in the presence of aerosols. The HONO signal was measured both with the lamp on and off for each aerosol surface area density to investigate the production of HONO from illuminated aerosol surfaces. The HONO signal was averaged over 50 s (average of 500 of the 355 nm photolysis laser pulses with a PRF of 10 Hz). Once aerosols were introduced into the flow tube system a period of ~

9

233 30 min was allowed for equilibration and the measured aerosol surface area density to stabilise.

234 In general, the relative humidity of the system was kept constant at RH ~ 15 % for all

235 experiments investigating HONO production as a function of NO_2 mixing ratio over the range

236 34 - 400 ppb. In a number of experiments, however, RH was varied in the range ~12-37 %.

237 The mixing ratio of NO_2 entering the flow tube was calculated using the concentration of the

238 NO_2 in the cylinder and the degree of dilution. The NO_2 mixing ratio within the cylinder was

239 determined using a commercial instrument based on UV-Vis absorption spectroscopy (Thermo

240 Fisher 42TL, limit of detection 50 pptv, precision 25 pptv) For each individual experiment, the

241 mixing ratio of NO_2 was kept constant (within the range 34 – 400 ppb) and the aerosol surface

242 area density was varied from zero up to a maximum of 0.04 $m^2\,m^{-3}$. In order to obtain the

243 HONO produced from illuminated aerosol surfaces in the flow tube for a given mixing ratio of

244 NO_2. As well as subtraction of any background HONO, a correction must be made for any loss

245 of HONO owing to its photolysis occurring within the flow tube.

246 In order to determine the rate of photolysis of HONO, the rate of photolysis of NO_2 was first

247 determined using chemical actinometry, and the known spectral output of the lamp and the

248 literature values of the absorption cross-sections and photo-dissociation quantum yields for

249 NO_2 and HONO were used to determine the rate of photolysis of HONO. When just flowing

250 NO_2 in the flow tube, the loss of NO_2 within the illuminated region is determined only by

251 photolysis and is given by:

$$-\frac{d[NO_2]}{dt} = j(NO_2)[NO_2] \tag{3}$$

252 where $j(NO_2)$ is the photolysis frequency of NO_2 for the lamp used in these experiments. From

253 the measured loss of NO_2 in the illuminated region, and with knowledge of the residence time,

254 the photolysis frequency, $j(NO_2)$, was determined to be $(6.43 \pm 0.30) \times 10^{-3}\,s^{-1}$ for the set of

255 experiments using one lamp to illuminate the flow tube. $j(NO_2)$ is given by:

$$j(NO_2) = \int_{\lambda_1}^{\lambda_2} \sigma_\lambda \phi_\lambda F_\lambda \, d\lambda \tag{4}$$

256 where λ_1 and λ_2 represent the range of wavelengths over which the lamp emits, and σ_λ and ϕ_λ

257 are the wavelength-dependent absorption-cross section and photo-dissociation quantum yield

258 of NO_2, respectively, and F_λ is the flux of the lamp at a given wavelength. The flux of the lamp,

259 the spectral intensity of which was measured using a Spectral Radiometer (Ocean Optics QE-
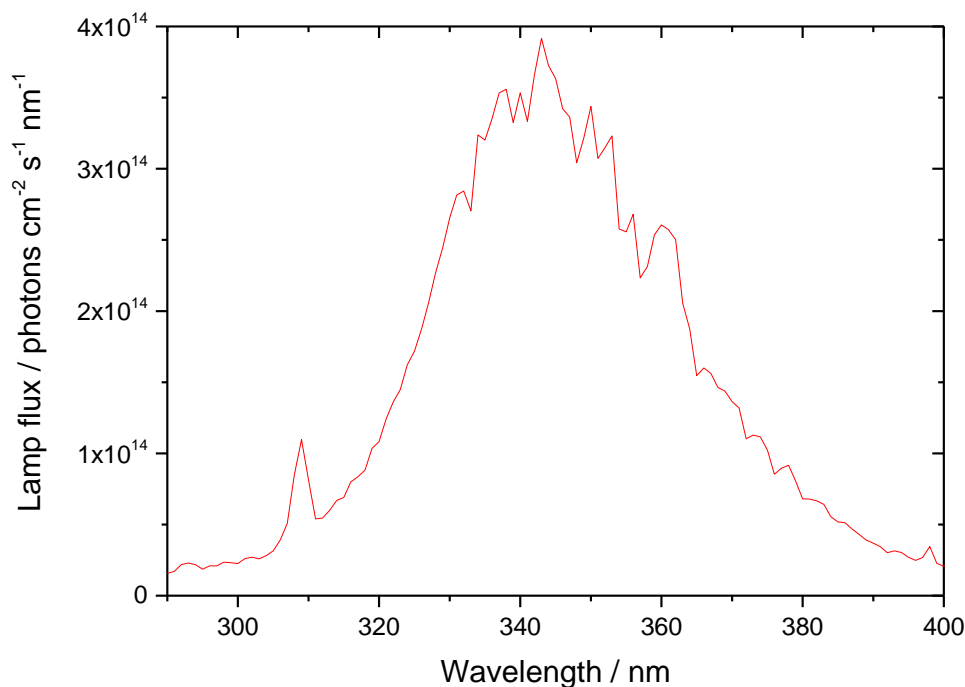260 Pro 500) as a function of wavelength, is shown in Figure 3.

Figure 3. UVA emission spectrum for the 15 W bench lamp used in these experiments between 290-400 nm. The integrated photon flux over this wavelength range is $(1.63 \pm 0.09) \times 10^{16}$ photons cm^{-2} s^{-1} determined from the measured $j(NO_2)$ of $(6.43 \pm 0.30) \times 10^{-3}$ s^{-1}.

261 From the measured $j(NO_2)$, and with knowledge of σ_λ and ϕ_λ for NO_2, the flux of the lamp was
262 determined to be $(1.63 \pm 0.09) \times 10^{16}$ photons cm^{-2} s^{-1} integrated over the $290 - 400$ nm
263 wavelength range of the lamp. Using this flux, and the known σ_λ and ϕ_λ for HONO over the
264 same wavelength range, $j(HONO)$ was determined to be $(1.66 \pm 0.10) \times 10^{-3}$ s^{-1}.

265 In the presence of aerosols under illuminated conditions, the rate of heterogeneous removal of
266 NO_2 at the aerosol surface to generate HONO is given by:

$$-\frac{d[NO_2]}{dt} = k[NO_2] \qquad (5)$$

267 where k is the pseudo-first order rate coefficient for loss of NO_2 at the aerosol surface, and
268 which leads to the generation of HONO. The postulated mechanism for HONO production
269 from NO_2 is discussed in section 3.3.2 below, but for the definition of k it is assumed to be a
270 first order process for NO_2. Integration of equation 5 gives:

$$k = -\frac{\ln(\frac{[NO_2]_0 - [HONO]_t}{[NO_2]_0})}{t} \quad (6)$$

271 where $[NO_2]_0 - [HONO]_t$ is the concentration of NO_2 at time t, assuming that each NO_2

272 molecule is quantitatively converted to a HONO molecule following surface uptake (see

273 section 3.3.2 for the proposed mechanism), and $[NO_2]_0$ is the initial concentration of NO_2.

274 Hence k can be determined from equation 6 using the measurement of the concentration of

275 HONO, [HONO], that has been generated from TiO_2 aerosol surfaces for an illumination time

276 of t (and after subtraction of any background HONO produced from other sources and after

277 correction for loss via photolysis, see above), and with knowledge of $[NO_2]_0$.

278 The reactive uptake coefficient of NO_2 to generate HONO, $\gamma_{NO_2 \rightarrow HONO}$, defined as the

279 probability that upon collision of NO_2 with the TiO_2 aerosol surface a gas-phase HONO

280 molecule is generated, is given by:

$$\gamma_{NO_2 \rightarrow HONO} = \frac{4 \times k}{v \times SA} \quad (7)$$

281 where v is the mean thermal velocity of NO_2, given by $v = \sqrt{(8RT/(\pi M)}$ with R, T and M as

282 the gas constant, the absolute temperature and the molar mass of NO_2, respectively, SA is the

283 aerosol surface area density ($m^2\,m^{-3}$) and k is defined as above. Rearrangement of equation 7

284 gives:

$$k = \frac{\gamma_{NO_2 \rightarrow HONO} \times SA \times v}{4} \quad (8)$$

285 Figure 4 shows the variation of k, determined from equation 6 above with $t = 52$ s (illumination

286 time in the flow tube), against aerosol surface area density, SA, for $[NO_2]_0 = 200$ ppb and

287 RH=15%, from which the gradient using equation 8 yields $\gamma_{NO_2 \rightarrow HONO} = (2.17 \pm 0.09) \times 10^{-5}$.
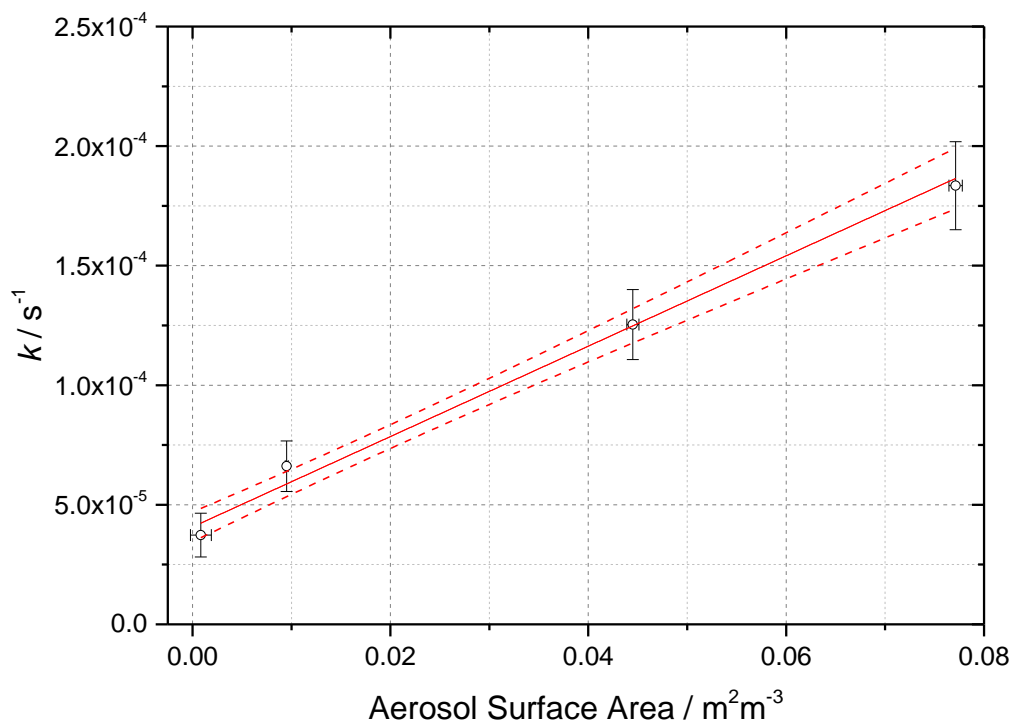
Figure 4. Pseudo-first-order rate coefficient for HONO production, k (open circles) as a function of aerosol surface area for $[NO_2]$ = 200 ppb and RH=15 ± 1 %, T = 293 ± 3 K and a photolysis time of 52 ± 2 seconds. The red line is a linear-least squared fit including 1σ confidence bands (dashed lines) weighted to both x and y errors (1σ), the gradient of which yields $\gamma_{NO_2 \to HONO}$ = (2.17 ± 0.09) × 10^{-5}, with the uncertainty representing (1σ). The non-zero y-axis intercept is due to a background HONO signal owing to the presence of a HONO impurity in the NO$_2$ cylinder, and which is not subtracted. The total photon flux of the lamp (see Figure 2 for its spectral output) = (1.63 ± 0.09) × 10^{16} photons cm^{-2} s^{-1}.

288   The uncertainty in k (~20 %) shown in Figure 4 and determined by equation 6 is mainly
289   controlled by the uncertainty in the HONO concentration (the HONO signal typically varies
290   between repeated runs for a given SA by ~ 10 % coupled with the 15 % error in calibration
291   factor), the initial NO$_2$ mixing ratio (10%), and the photolysis time, t (~3 %). The uncertainty
292   in SA is determined by the uncertainty in the SMPS (15%). The error in the value of
293   $\gamma_{NO_2 \to HONO}$ (typically 20%) is calculated from the 1σ statistical error of the weighted fit shown
294   in Figure 4. An experiment performed using air yielded an uptake coefficient value within 7 %
295   of the equivalent experiment done in N$_2$, which is well within the experimental error.

296   ## 2.5   Box model description

297   A kinetic scheme within the framework of a box model was used together with the differential
298   equation solver Facsimile 4.3.53 (MCPA software Ltd., 2020) to investigate the mechanism of

13

299   NO$_2$ adsorption on TiO$_2$ in the presence of light to produce HONO. The models were only

300   semi-explicit, focusing on determining the stoichiometric amounts of NO$_2$ needed to produce

301   a single HONO molecule in the gas-phase for comparison with the experimental dependence

302   of HONO production upon NO$_2$ mixing ratio, and to provide a predictive framework for

303   parameterising the HONO production rate with NO$_2$ mixing ratio in the atmosphere. Three

304   model scenarios were designed. The simplest model (Model 1) considered only the adsorption

305   of a single molecule of NO$_2$ to the TiO$_2$ surface, the surface conversion to HONO in the

306   presence of light and subsequent desorption of HONO, the latter assumed to occur rapidly. The

307   two further model scenarios investigated the effect of a 2:1 stoichiometric relationship between

308   the NO$_2$ adsorbed to the surface of TiO$_2$ and the HONO produced, via the formation of an NO$_2$

309   dimer. Model 2 incorporated an Eley-Rideal mechanism reliant on the adsorption of one NO$_2$

310   molecule to the surface followed by the subsequent adsorption of a second NO$_2$ molecule

311   directly onto the first (Figure 5). Model 3, however, features a Langmuir-Hinshelwood

312   mechanism of adsorption in which two NO$_2$ molecules adsorb to the surface, then diffuse to

313   one another before colliding on the surface and forming the *cis*-ONO-NO$_2$ dimer (Finlayson-

314   Pitts et al., 2003;de Jesus Madeiros and Pimentel, 2011;Liu and Goddard, 2012;Varner et al.,

315   2014). The formation of the asymmetric *cis*-ONO-NO$_2$ dimer followed by isomerisation to

316   form the asymmetric *trans*-ONO-NO$_2$ dimer has been suggested to have an enthalpic barrier

317   that is ~170 kJ mol^{-1} lower than for direct isomerisation to *trans*-ONO-NO$_2$ from the symmetric

318   N$_2$O$_4$ dimer (Liu and Goddard, 2012). The dimerisation of NO$_2$ and subsequent isomerisation

319   to form *trans*-ONO-NO$_2$ has been suggested under dark conditions to lead to the formation of

320   both HONO and HNO$_3$ in the presence of water vapour (Finlayson-Pitts et al., 2003;de Jesus

321   Madeiros and Pimentel, 2011;Liu and Goddard, 2012;Varner et al., 2014). Although the

322   interaction of light with TiO$_2$ with the concomitant production of electron-hole pairs (R1) is

323   central to HONO formation, we do not specify here the exact mechanism by which the electron-

324   hole pairs interact with surface-bound species to generate HONO. We propose that the

325   interaction with light speeds up the autoionisation of *trans*-ONO-NO$_2$ to form (NO$^+$)(NO$_3^-$),

326   which is represented by reactions R13 and R15 in Models 2 and 3 respectively. (NO$^+$)(NO$_3^-$)

327   can then react rapidly with surface adsorbed water leading to HONO formation (Varner et al.,

328   2014).

329   A schematic of the proposed mechanism investigated with Models 2 and 3 is shown in Figure

330   5, and consists of (i) the adsorption of NO$_2$ onto a surface site, (ii) the conversion of NO$_2$ to

331   form HONO via the formation of an NO$_2$ dimer intermediate on the surface via either a Eley-

14

332 Rideal or Langmiur Hinshelwood- type mechanism, (iii) subsequent desorption of HONO from

333 the surface, and finally (iv) competitive removal processes for HONO both on the surface and

334 in the gas-phase that are either dependent or independent on the NO_2 mixing ratio. The model

335 includes the gas-phase photolysis of NO_2 and HONO and the gas phase reactions of both
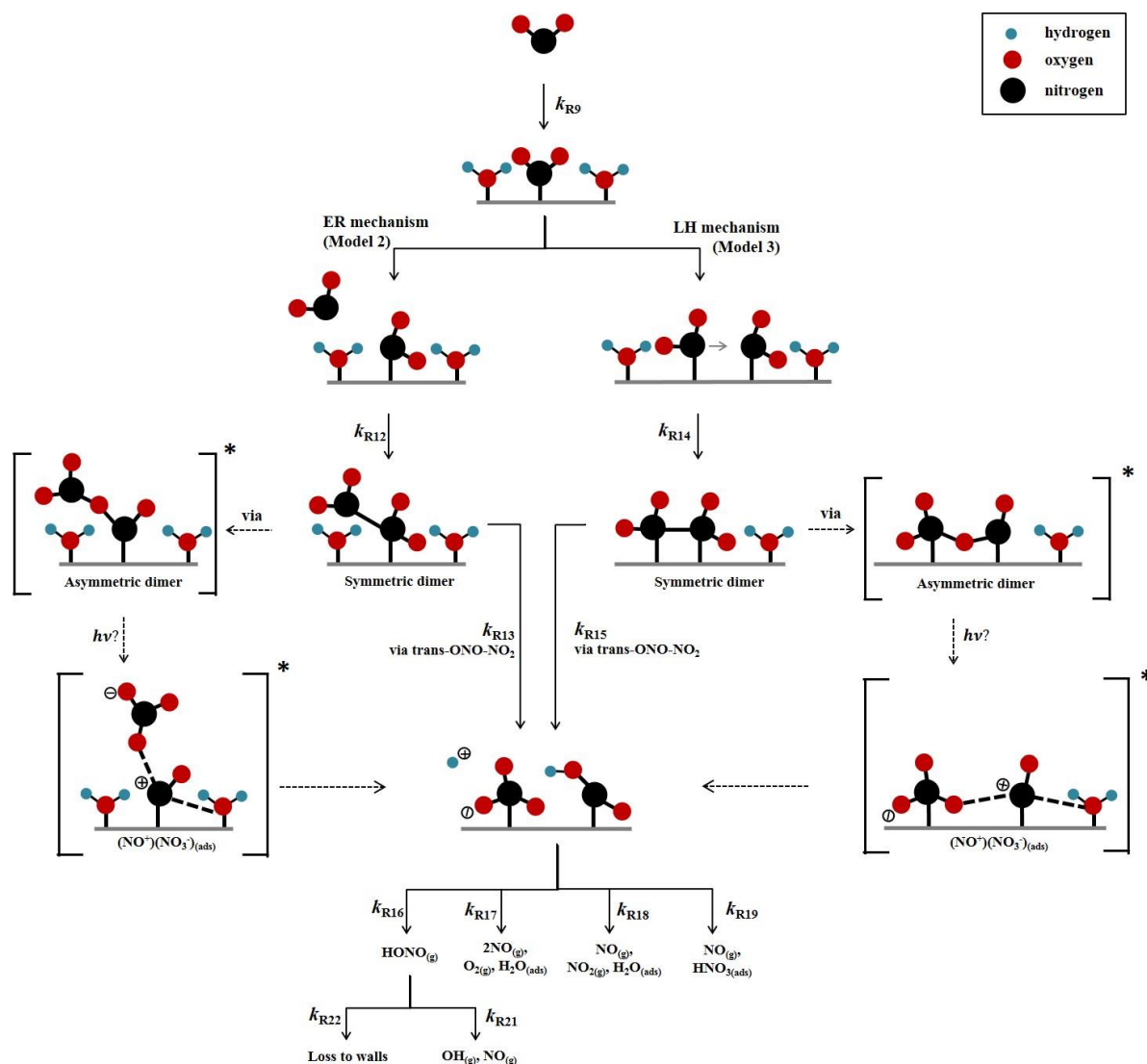
336 HONO and NO_2 with OH and $O(^3P)$ atoms.

Figure 5. Schematic diagram of proposed mechanism of uptake of NO_2 on an aerosol surface in the presence of water to form HONO. Both Eley Rideal, Model 2, and Langmuir Hinshelwood, Model 3, mechanisms are shown with relevant estimated and calculated rate coefficients used in the models. NO_2 dependent and independent loss reactions of HONO are also depicted. Nitrogen shown in black, oxygen shown in red and hydrogen shown in blue. * denotes intermediate steps of the isomerisation of symmetric N_2O_4 to *trans*-ONO-NO_2 which is then predicted to form HONO.

337 To the best of our knowledge the enthalpy of adsorption of NO_2 onto a TiO_2 surface has not

338 been determined, nor the bimolecular rate coefficients for the chemical steps on the surface

339 shown in Figure 5. Hence, for each of the steps a rate coefficient (s^{-1} or cm^3 molecule^{-1} s^{-1}) was

340 assigned, as given in Table 1, and with the exception of the experimentally determined $j(NO_2)$

341 and the calculated $j(HONO)$, and the gas-phase rate coefficients which are known, the rate

342 coefficients were estimated, with the aim of reproducing the experimental NO_2 dependence of

343 the HONO production and NO_2 reactive uptake coefficient; justification of chosen values is

344 given below.

Reactions	Rate coefficient[d]
Model 1	
R9 $NO_{2(g)} + surface \rightarrow NO_{2(ads)}$	1×10^{-3}
R10 $NO_{2(ads)} \rightarrow HONO_{(ads)}$	1×10^{-3}
R11 $HONO_{(ads)} \rightarrow HONO_{(g)}$	1×10^{-2}
Model 2 and 3	
Model 2 only – Eley-Rideal mechanism	
R12 $NO_{2(g)} + NO_{2(ads)} \rightarrow NO_2 - NO_{2(ads)}$	1×10^{-2}
R13 $NO_2 - NO_{2(ads)} \xrightarrow{via\ trans-ONO-NO_2} HONO_{(ads)} + HNO_{3(ads)}$	5×10^{-3}
Model 3 only – Langmuir-Hinshelwood mechanism	
R14 $NO_{2(ads)} + NO_{2(ads)} \rightarrow NO_{2(ads)} - NO_{2(ads)}$	1×10^{-3}
R15 $NO_{2(ads)} - NO_{2(ads)} \xrightarrow{via\ trans-ONO-NO_2} HONO_{(ads)} + HNO_{3(ads)}$	5×10^{-3}
Common to both Models 2 and 3	
R9 $NO_{2(g)} + surface \rightarrow NO_{2(ads)}$	1×10^{-1}
R16 $HONO_{(ads)} \rightarrow HONO_{(g)}$	5×10^{-2}
R17 $HNO_{3(ads)} + HONO_{(ads)} \rightarrow 2NO_{(g)} + O_{2(g)} + H_2O_{(ads)}$	1×10^{-3}
R18 $HONO_{(ads)} + HONO_{(ads)} \rightarrow NO_{(g)} + NO_{2(g)} + H_2O_{(ads)}$	1×10^{-3}
R19 $NO_{2(g)}(or\ species\ such\ as\ NO_2^+) + HONO_{(ads)} \rightarrow NO_{(g)} + HNO_{3(ads)}$	5×10^{-3}
R20 $NO_{2(g)} + h\nu \rightarrow NO_{(g)} + O(^3P)_{(g)}$	6×10^{-3a}
R21 $HONO_{(g)} + h\nu \rightarrow OH_{(g)} + NO_{(g)}$	2×10^{-3b}
R22 $HONO_{(g)} \rightarrow wall\ loss$	1×10^{-4}
R23 $HONO_{(g)} + OH_{(g)} \rightarrow NO_{2(g)} + H_2O_{(g)}$	4.5×10^{-12c}
R24 $NO_{2(g)} + OH_{(g)} \xrightarrow{M} HNO_{3(g)}$	1×10^{-11c}
R25 $O(^3P)_{(g)} + NO_{2(g)} \rightarrow O_{2(g)} + NO_{(g)}$	1×10^{-11c}
R26 $O(^3P)_{(g)} + O_{2(g)} \xrightarrow{M} O_3$	1.5×10^{-14c}
R27 $O(^3P)_{(g)} + NO_{(g)} \xrightarrow{M} NO_{2(g)}$	1.7×10^{-12c}

345 **Table 1.** Reactions included in the chemical mechanism used to model NO_2 uptake onto TiO_2 aerosols. All rate

346 coefficients are estimated, as described in Section 2.5, with the exception of the NO_2 and HONO photolysis rate

347 coefficient and the gas phase rate coefficient which are known. [a]Measured using chemical actinometry with the

352   The modelled Gibbs free energy barrier for the isomerisation of N_2O_4 to form the asymmetric

353   ONO-NO_2 isomer (*cis* or *trans* conformation not specified) was estimated by Pimental et al.,

354   (2007) to be 87 kJ mol^{-1} with a rate coefficient as large as 2×10^{-3} s^{-1} in the aqueous phase at

355   298 K, stated in the study to confirm the Finlayson-Pitts model for the hydrolysis of NO_2 on

356   surfaces via the asymmetric *trans*-ONO-NO_2 dimer (Finlayson-Pitts et al., 2003). Using this

357   study as a guide, we estimated k_{R13} and k_{R15} as 5×10^{-3} s^{-1}, slightly larger than that estimated

358   by Pimental et al., (2007) due to the presence of light. A study into the decomposition of HONO

359   on borosilicate glass surfaces suggested a rate coefficient for the loss HONO on the non-

360   conditioned chamber walls to be $(1.0 \pm 0.2) \times 10^{-4}$ s^{-1} increasing to $(3.9 \pm 1.1) \times 10^{-4}$ s^{-1} when

361   HNO_3 was present on the walls (Syomin and Finlayson-Pitts, 2003). From this we estimated a

362   light-accelerated loss rate coefficient of 1×10^{-3} s^{-1} for the loss of HONO$_{(ads)}$ by reaction with

363   itself, k_{R18}, and through reaction with $HNO_3{}_{(ads)}$, k_{R17}. Both these reactions will occur on the

364   surface of the aerosol. We make the assumption that the rate of loss of HONO to the walls of

365   the chamber for this experiment is less than that of the heterogeneous loss reactions on the

366   photo-catalytic aerosol surface leading to a k_{R22} of 1×10^{-4} s^{-1} as reported by (Syomin and

367   Finlayson-Pitts, 2003). For k_{R12}-k_{R15}, initial values were adopted and were then adjusted to fit

368   the shape of the trend in experimental results of [HONO] and $\gamma_{NO_2 \rightarrow HONO}$ versus [NO_2],

369   discussed fully in Section 3.3.2. For completeness, gas-phase loss reactions of HONO and NO_2

370   with OH and the reactions of O(^{3}P) with NO, NO_2 and O_2 were also included in the model,

371   R23-R27, though their inclusion had no effect on the HONO concentration. The rates of R23-

372   R27 within the model are much smaller than HONO loss reactions on the surface (R17-R19)

373   and the photolysis reactions (R21). For both Models 2 and 3, the adsorption of an NO_2 molecule

374   to the surface, k_{R9}, was assumed to be rapid and not the rate determining step. Likewise, the

375   desorption of HONO was also assumed to be rapid, faster than the loss rates of adsorbed HONO

376   but slower than the adsorption of NO_2; this was necessary for the model to reproduce the trend

377   in the experimental results of [HONO] versus [NO_2], discussed fully in Section 3.3.2.

3   Results and Discussion

3.1   HONO production from TiO_2 aerosol surfaces in the presence of NO_2

The production of HONO on TiO_2 aerosol surfaces was measured as a function of the initial NO_2 mixing ratio. Figure 6 shows the dependence of the HONO concentration, measured at the end of the flow tube, on the initial NO_2 mixing ratio for an aerosol surface area of $(1.6 \pm 0.8) \times 10^{-2}$ m^2 m^{-3}. A sharp increase in HONO production at a low mixing ratio of NO_2 was seen followed by a more gradual reduction in HONO production after a peak production at ~ 54 ± 5 ppb NO_2.
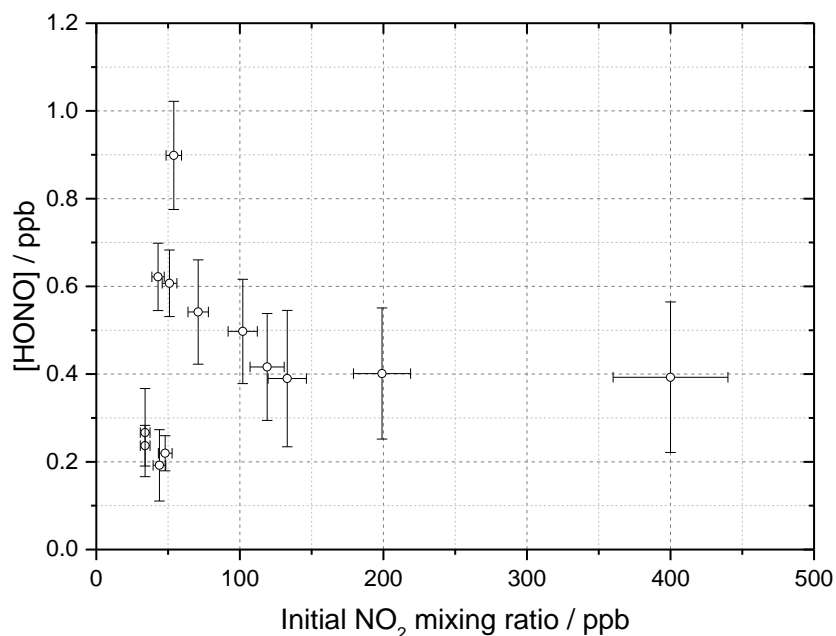

Figure 6. HONO concentration measured at the end of the flow tube as a function of the initial NO_2 mixing ratio, for the aerosol surface area density of $(1.6 \pm 0.8) \times 10^{-2}$ m^2 m^{-3}, relative humidity 15 ± 1 %, photon flux $(1.63 \pm 0.09) \times 10^{16}$ photons cm^{-2} s^{-1} (290-400 nm wavelength range), reaction time of 52 seconds and N_2 carrier gas. Each point is an average of up to 20 measurements at the same aerosol surface area and mixing ratio of NO_2. The highest concentration of HONO measured was 0.90 ± 0.12 ppb at $[NO_2] = 54 \pm 5$ ppb. The y error bars represent 1σ while the x error bars represent the sum in quadrature of the errors in the N_2 and NO_2 gas flows and the NO_2 dilution. The SA varied over the experiments at different NO_2 mixing ratios leading to a larger error in the quoted SA.

Figure 7 shows the HONO concentration measured at the end of the flow tube over a range of RH values for a fixed aerosol surface area density of $(1.59 \pm 0.16 \times 10^{-2}$ m^2 $m^{-3})$ and at two

18

388   NO_2 mixing ratios, displaying a peak in HONO production between 25 – 30 % RH. Above ~

389   37 % RH, for experiments including single-component TiO_2 aerosols, it was found that

390   significant aerosols were lost from the system before entering the flow tube, speculated to be

391   due to loss to the walls of the Teflon lines. As such the RH dependence was only studied up to

392   37 % RH, however a clear drop off in HONO production was seen for both NO_2 mixing ratios
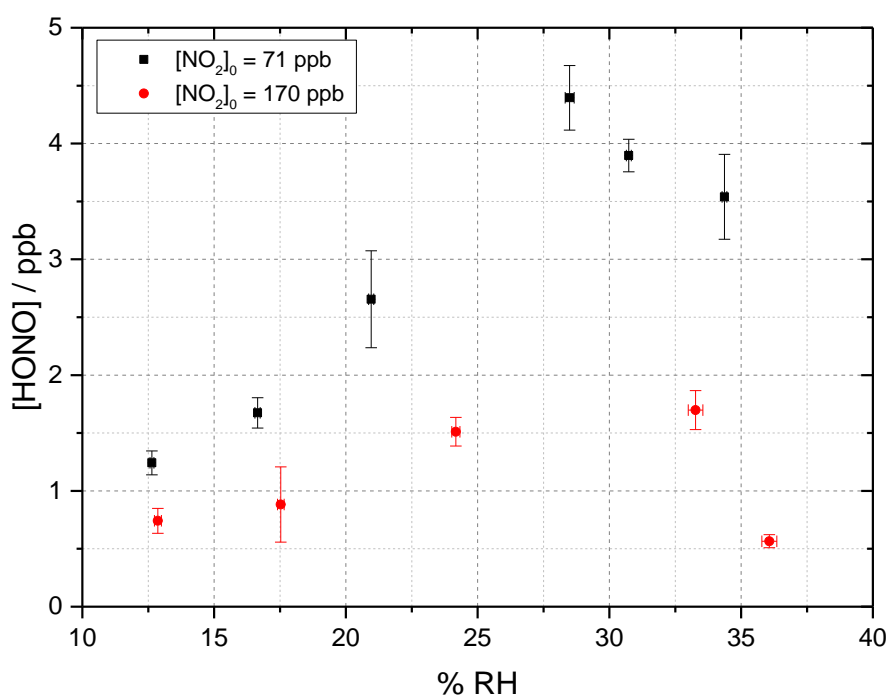
393   studied after ~ 30 % RH.

Figure 7. RH dependence of HONO production from illuminated TiO_2 aerosol surfaces at 295 K in N_2 at 71 (black) and 170 (red) ppb initial NO_2 mixing ratio. The aerosol surface area density was kept constant at $(1.59 \pm 0.16) \times 10^{-2}$ $m^2\,m^{-3}$ with a photon flux of $(1.63 \pm 0.09) \times 10^{16}$ photons $cm^{-2}\,s^{-1}$ and an illumination time of 52 ± 2 seconds. The error bars represent 1σ.

394   A dependence of HONO production upon RH was expected due to the potential role of water

395   as a proton donor in the production mechanism of HONO on TiO_2 surfaces (R2 and (R5, as

396   shown in Figure 5 (Dupart et al., 2014). The fractional surface coverage of water on the TiO_2

397   aerosol core, V/V_m, at 15 % RH and above was calculated using the parameterisation below,

398   which was determined using transmission IR spectroscopy (Goodman et al., 2001):

$$\frac{V}{V_m} = \left[\frac{c\left(\frac{P}{P_0}\right)}{1 - \left(\frac{P}{P_0}\right)} \right] \left[\frac{1 - (n+1)\left(\frac{P}{P_0}\right)^n + n\left(\frac{P}{P_0}\right)^{n+1}}{1 + (c-1)\left(\frac{P}{P_0}\right) - c\left(\frac{P}{P_0}\right)^{n+1}} \right] \tag{9}$$

399   where V is the volume of water vapour adsorbed at equilibrium pressure P, V_m is the volume

400   of gas necessary to cover the surface of TiO_2 particles with a complete monolayer, P_0 is the

401   saturation vapour pressure, c is the temperature dependent constant related to the enthalpies of

402   adsorption of the first and higher layers (taken as 74.8 kJ mol^{-1} for TiO_2 (Goodman et al., 2001))

403   and n is the asymptotic limit of monolayers (8 for TiO_2 (Goodman et al., 2001)) at large values

404   of P/P_0.

405   At 15 % RH, a fractional water coverage of 1.09 was calculated to be present on the surface,

406   increasing to 1.50 at 35 % RH. It has been shown in previous work that HONO can be displaced

407   from a surface by water, leading to an increase in gas-phase HONO with RH (Syomin and

408   Finlayson-Pitts, 2003). The increase in HONO with RH to ~25-30 % RH could therefore be

409   attributed to both an increase in the concentration of the water reactant leading to more HONO

410   formation and the increase in displacement of HONO from the surface due to preferential

411   adsorption of water. A decrease in HONO production seems to occur above ~ 30 % RH, which

412   could be due to the increased water adsorption inhibiting either NO_2 adsorption or the

413   electron/hole transfer process (Gustafsson et al., 2006). H_2O vapour adsorption is likely

414   enhanced by the superhydrophilic properties of TiO_2 surfaces under UV radiation meaning that

415   water monolayers form more quickly on the surface of TiO_2 owing to light-induced changes in

416   surface tension (Takeuchi et al., 2005;Gustafsson et al., 2006).

417   At the higher initial concentration of NO_2 = 170 ppb, the RH dependence showed a similar

418   peak in HONO production between ~25 - 30 % RH but less HONO was produced overall, as

419   expected from Figure 6 given the higher NO_2. Previous work on the production of HONO from

420   suspended TiO_2 aerosols reported a strong RH dependence of the uptake coefficient, γ, of NO_2

421   to form HONO with a peak at ~ 15 % RH and decreasing at larger RH (Gustafsson et al., 2006).

422   The same trend for the NO_2 uptake coefficient was observed by Dupart et al., 2014 on Arizona

423   test dust (ATD) aerosols with a peak in γ at ~ 25 % RH. This increase in the RH at which the

424   uptake coefficient for NO_2 in going from TiO_2 to ATD aerosols was ascribed to the lower

425   concentration of TiO_2 present in ATD aerosols as opposed to single-component TiO_2 aerosols

426   used by Gustafsson et al., 2006 as well as by differences in particle size distribution. Gustafsson

427   et al., 2006 reported a larger aerosol size distribution with a bimodal trend with mode diameters

428 of ~ 80 and ~ 350 nm for single-component TiO_2 aerosols whereas Dupart et al., 2014 reported

429 a smaller unimodal aerosol size distribution for ATD aerosols with a mode diameter of ~110

430 nm. In this work we also see a larger aerosol size distribution, with a lower mode diameter of

431 ~ 180 nm similar to Dupart et al., 2014 but for pure TiO_2 aerosols; aerosol size distribution

432 shown in Figure 2. Similar to the results of Dupart et al., 2014 we observe a trend inversion in

433 [HONO] vs RH at higher RH, between 25-30 %. An increase in HONO as a function of RH

434 has also been observed on TiO_2 containing surfaces (Langridge et al., 2009;Gandolfo et al.,

435 2015;Gandolfo et al., 2017) with a similar profile for the observed RH dependence of HONO

436 being observed by Gandolfo et al., (2015) from photo-catalytic paint surfaces with a maximum

437 in HONO mixing ratio found at 30 % RH. In comparison, a study focusing on the products of

438 the uptake of NO_2 on TiO_2 surfaces showed a maximum in the gas-phase HONO yield at 5 %

439 RH with the yield of HONO plateauing off with further increase in humidity (Bedjanian and

440 El Zein, 2012).

441 **3.2   Dependence of reactive uptake coefficient on initial NO_2 mixing ratio**

442 The reactive uptake coefficient, $\gamma_{NO_2 \rightarrow HONO}$ for $NO_2 \rightarrow HONO$ on TiO_2 aerosol particles was

443 determined experimentally for 18 different initial NO_2 mixing ratios, and is shown in Figure 8.

444 For each initial NO_2 mixing ratio, the gradient of the first order rate coefficient for HONO

445 production, *k*, as a function of aerosol surface area density (e.g. Figure 4) and in conjunction

446 with equation 8, was used to obtain $\gamma_{NO_2 \rightarrow HONO}$. The uptake coefficient initially increases with

447 NO_2, reaching a peak at $\gamma_{NO_2 \rightarrow HONO}$ = $(1.26 \pm 0.17) \times 10^{-4}$ for an initial NO_2 mixing ratio of

448 51 ± 5 ppb, before sharply decreasing as the NO_2 mixing ratio continues to increase above this
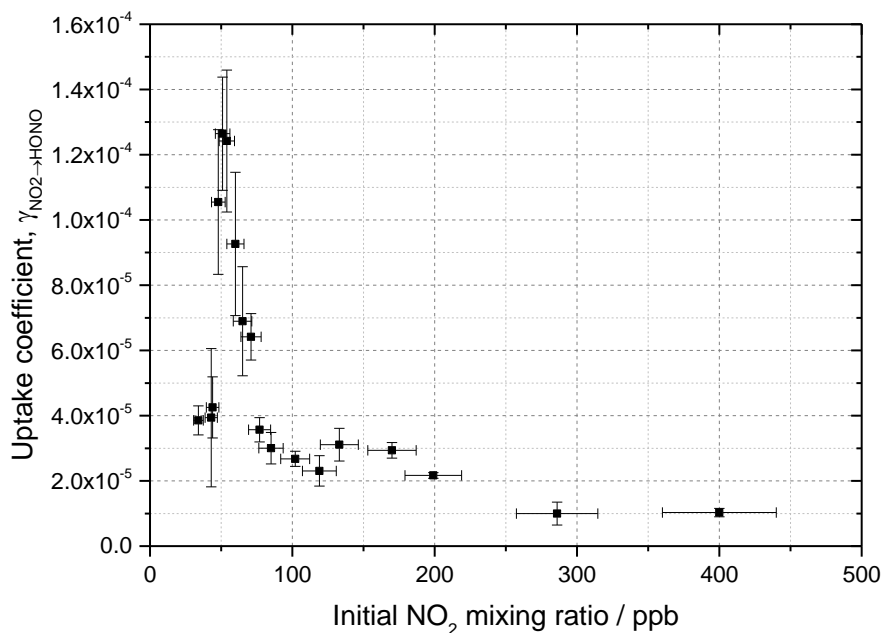
449 value.

Figure 8 Experimental results showing the reactive uptake coefficients of NO_2 to form HONO, $\gamma_{HONO \rightarrow NO_2}$ onto TiO_2 aerosol surfaces as a function of the initial NO_2 mixing ratio. All experiments were conducted in N_2 at 295 K at 15 ± 1 % RH, a photon flux of $(1.63 \pm 0.09) \times 10^{16}$ photons cm^{-2} s^{-1} and an illumination time of 52 ± 2 seconds. $\gamma_{HONO \rightarrow NO_2}$ was determined for each NO_2 mixing ratio from the gradient of the pseudo-first-order rate coefficient for HONO production, k, versus aerosol surface area density varied from 0 - 0.04 m^2 m^{-3} (e.g. as shown in Figure 4) and equation 8.

450   The increase in uptake coefficient with NO_2 at low NO_2 (< 51 ppb) has not been seen previously
451   in studies of HONO production from TiO_2 containing aerosols with similar [NO_2] ranges
452   (Gustafsson et al., 2006;Ndour et al., 2008;Dupart et al., 2014) nor with other aerosol surfaces
453   (Bröske et al., 2003;Stemmler et al., 2007) or TiO_2 surfaces (El Zein and Bedjanian, 2012b). It
454   is worth noting that several of these studies reported the overall uptake of NO_2 onto aerosol
455   surfaces and not specifically the uptake to form HONO, although HONO was indirectly
456   measured in all studies noted here (Gustafsson et al., 2006;Ndour et al., 2008;Dupart et al.,
457   2014). For single-component TiO_2 aerosols, Gustafsson et al., (2006) reported a uptake
458   coefficient, γ_{NO_2}, of 9.6×10^{-4} at 15 % RH and 100 ppb NO_2. Taking into account the HONO
459   yield of 0.75 given by (Gustafsson et al., 2006), an estimated $\gamma_{NO_2 \rightarrow HONO} = 7.2 \times 10^{-4}$ is
460   determined and can be compared to the value observed in this work at 15 % RH and 100 ppb
461   NO_2, ($\gamma_{NO_2 \rightarrow HONO} = (2.68 \pm 0.23) \times 10^{-5}$). The $\gamma_{NO_2 \rightarrow HONO}$ we determine is 27 times smaller
462   than reported by Gustafsson et al., (2006). This difference is mostly due to the lower
463   experimental photon flux in our setup, ~19 times less at $\lambda_{max} = 365$ nm owing to the use of

22

464 one 15 W UV lamp to irradiate the flow tube (Boustead, 2019) compared to Gustafsson et al.,
465 2006 which utilised four 18 W UV lamps.

466 The origins of the increase in $\gamma_{NO_2 \rightarrow HONO}$, together with reaching a maximum and the
467 subsequent decrease at larger NO_2 mixing ratios was investigated using the kinetic box model
468 and postulated mechanism for HONO production described in Section 2.5. The aim was to
469 compare the observed production of HONO and $\gamma_{NO_2 \rightarrow HONO}$ with the modelled values, as a
470 function of NO_2 mixing ratio. The skill of the model to reproduce the observed behaviour
471 enables a validation of the postulated mechanism for HONO production, and variation of the
472 kinetic parameters enables the controlling influence of different steps in the mechanism on
473 HONO production to be evaluated.

3.3 Modelling the HONO production mechanism on illuminated TiO_2 aerosol surfaces

476 The HONO production on illuminated TiO_2 aerosol surfaces was investigated for each of the
477 mechanisms outlined in Table 1.

3.3.1 Model 1

479 Model 1 (see Table 1 and Figure 5), which contains the simplest mechanism, was designed to
480 reproduce the decreasing value of the NO_2 uptake coefficient to form HONO, $\gamma_{NO_2 \rightarrow HONO}$, with
481 increasing NO_2 and also the plateauing at higher NO_2 mixing ratios caused by NO_2 reaching a
482 maximum surface coverage, as seen by Stemmler et al., (2007). A decrease in the uptake
483 coefficient of NO_2, γ_{NO_2}, onto dust aerosol surfaces was also seen in studies where the
484 formation of HONO from NO_2 uptake was not directly studied (Ndour et al., 2008;Dupart et
485 al., 2014). The mechanism for Model 1 which is given in Table 1 describes the adsorption of
486 one NO_2 molecule to a surface site which then undergoes the reaction which forms HONO,
487 followed by desorption of HONO to the gas-phase, R9-R11. Any representation of the specific
488 chemical processes which convert NO_2 to HONO on the surface following the initial photo-
489 production of electron-hole pairs in the TiO_2 structure (R2) was not included here as the
490 primary focus was to produce the relationship between $\gamma_{NO_2 \rightarrow HONO}$ and the NO_2 mixing ratio.
491 Gustafsson et al., (2006) reported that the measured rate of photo-induced HONO production
492 is 75% that of the rate of NO_2 removal, whereas the dark disproportionation reaction (R28)
493 would predict a 50% yield, and hence that the HONO observed in their studies is not simply a
494 photo-enhancement of:

$$2NO_{2(ads)} + H_2O_{(ads)} \rightarrow HONO_{(g)} + HNO_{3(ads)} \tag{R28}$$
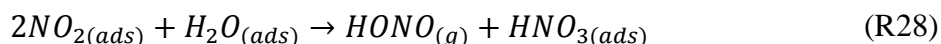
495 Gustafsson et al., (2006) suggests that an oxidant on the surface is produced following the

496 creation of the electron-hole pair (OH is generated in (R2)), and suggests H_2O_2 as a possibility,

497 which is consistent with the observation of OH and HO_2 radicals produced from the surface of

498 illuminated TiO_2 aerosols (Moon et al., 2019). For Model 1, outputs for the predicted

499 concentration of HONO and the reactive uptake coefficient, $\gamma_{NO_2 \rightarrow HONO}$, as a function of initial

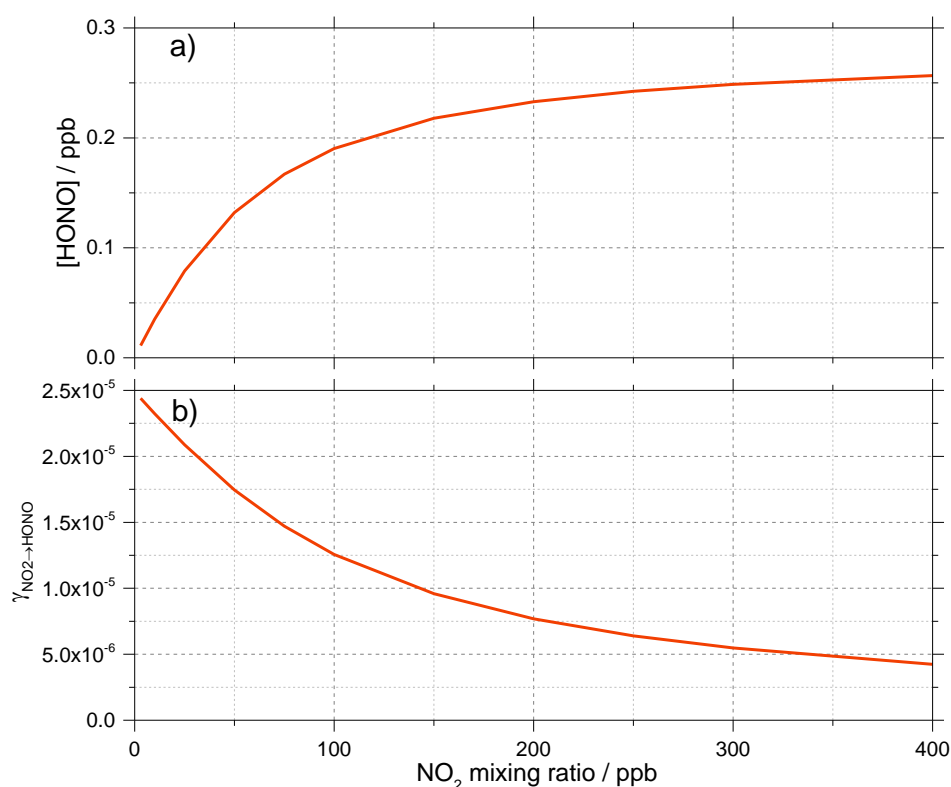500 NO_2 mixing ratio are shown in Figure 9.

Figure 9 Model 1 calculations for (a) the concentration of HONO and (b) the reactive uptake coefficient to

form HONO, $\gamma_{NO_2 \rightarrow HONO}$, as a function of NO_2 mixing ratio for a model run time of 52 s. The estimated rate

coefficients used in this model are shown in Table 1.

501 For a run time of 52 s, equal to that of the experimental illumination time, Model 1 predicts an

502 increase in HONO production with increasing NO_2 mixing ratio until the HONO concentration

503 begins to plateau, reaching ~0.25 ppb at $[NO_2]$ = 400 ppb, presumably owing to saturation on

504 active aerosol surface sites by NO_2. This leads to the modelled reactive uptake coefficient,

505 $\gamma_{NO_2 \rightarrow HONO}$, monotonically decreasing with increasing NO_2 mixing ratio; a variation in NO_2

506 uptake coefficient similar to that seen in previous photo-enhanced NO_2 aerosol uptake studies

507 (Bröske et al., 2003;Stemmler et al., 2007;Ndour et al., 2008;Dupart et al., 2014). However,

508　the model predictions for Model 1 do not reproduce the experimental variations shown in
509　Figure 6 and Figure 8, in which there is an observed initial rise and then a fall in both the
510　HONO concentration and $\gamma_{NO_2 \to HONO}$ with increasing NO_2 mixing ratio. Hence, additional
511　processes were considered in the model in order to try to reproduce this behaviour.

512　**3.3.2　Models 2 and 3. Investigating the role of NO_2 dimerisation for the surface**
513　**formation of HONO, and including additional surface losses of HONO**

514　As the experimental $\gamma_{NO_2 \to HONO}$ increases with NO_2 at low NO_2 (Figure 8), we postulate in
515　Models 2 and 3 that the production of HONO under illuminated conditions is not fully first
516　order in NO_2 and requires more than one NO_2 molecule to form HONO, consistent with the
517　formation of the symmetric NO_2 dimer (N_2O_4) followed by isomerisation on the surface to
518　form the asymmetric *trans*-ONO-NO_2 dimer, which has been suggested to be more reactive
519　with water than the symmetric N_2O_4 dimer (Finlayson-Pitts et al., 2003;Ramazan et al.,
520　2004;Ramazan et al., 2006;Liu and Goddard, 2012) due to the autoionisation to form
521　$(NO^+)(NO_3^-)$ which we propose is accelerated by the presence of light; the full mechanism for
522　which is shown in Figure 5. A recent rotational spectroscopy study found that the *trans*-ONO-
523　NO_2 was better described as the ion pair $(NO^+)(NO_3^-)$ (Seifert et al., 2017). Reaction of the
524　$(NO^+)(NO_3^-)$ ion pair with surface adsorbed water can then lead to the formation of HONO and
525　HNO_3, the feasibility of which is supported by molecular dynamics simulation studies (Varner
526　et al., 2014). While the symmetric N_2O_4 dimer is favoured as it is the most stable conformer,
527　the asymmetric forms have been experimentally observed in several studies (Fateley et al.,
528　1959;Givan and Loewenschuss, 1989b, a, 1991;Pinnick et al., 1992;Forney et al., 1993;Wang
529　and Koel, 1998, 1999;Beckers et al., 2010). A more recent *ab initio* study of NO_2 adsorption
530　at the air-water interface suggested an orientational preference of NO_2 on the surface, with both
531　oxygen atoms facing away from the interface which may imply that the asymmetric dimer
532　ONO-NO_2 can form directly, meaning the high barrier between the symmetric and asymmetric
533　forms does not need to be overcome (Murdachaew et al., 2013).

534　The energy barrier to isomerisation of symmetric N_2O_4 in the gas-phase may be reduced due
535　to the interaction with water adsorbed on surfaces. We therefore rule out the dimer in the gas-
536　phase adsorbing onto the surface first, and then reacting to form HONO (Varner et al., 2014).
537　An interesting question is whether the first NO_2 molecule adsorbed to the surface dimerises via
538　the addition of a gaseous NO_2 via an Eley-Rideal (ER) type process, or whether a Langmuir-
539　Hinshelwood (LH) type mechanism is operating in which both NO_2 molecules are first

540   adsorbed and then diffuse together on the surface forming N_2O_4. Both ER and LH mechanisms

541   to form the NO_2 dimer have been included in the model, denoted as Model 2 and Model 3,

542   respectively. The outputs for Models 2 and 3 (see Table 1 for details of the processes included)

543   for the HONO concentration and $\gamma_{NO_2 \rightarrow HONO}$ as a function of NO_2 are shown in Figure 10

544   together with the experimental data. The stoichiometric relationship of the requirement of two

545   NO_2 molecules forming HONO on the surface was key to reproducing the experimental trend

546   of first an increase and then a decrease in both the HONO concentration and the reactive uptake

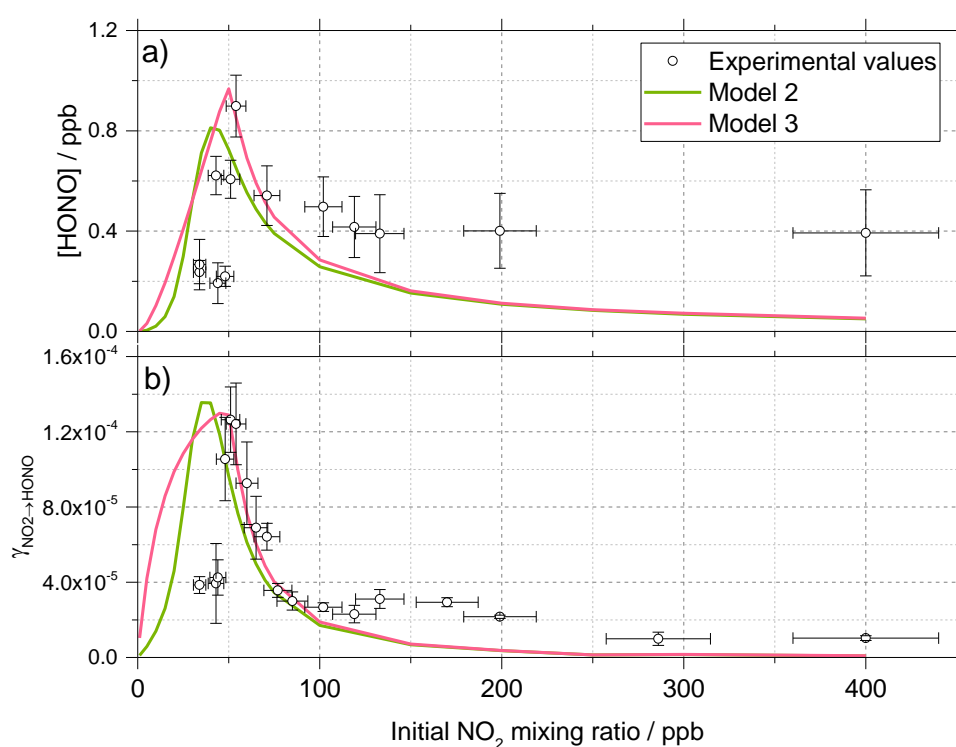547   coefficient with the initial NO_2 mixing ratio.

Figure 10. Experimental values (open circles with 1σ error bars), Model 2 (green line) and Model 3 (pink line) calculations for (a) HONO concentration after 52 s illumination and (b) NO_2 reactive uptake coefficient, $\gamma_{NO_2 \rightarrow HONO}$, as a function of the initial NO_2 mixing ratio. The mechanisms used for these model runs included a 2:1 stoichiometric relationship between the NO_2 adsorbed on the TiO_2 aerosol surface and the HONO produced, as well as additional HONO loss reactions which are dependent on NO_2, see Table 1 for details. Models 2 and 3 use an Eley-Rideal and Langmuir-Hinshelwood mechanisms, respectively, for the formation of the NO_2 dimer on the aerosol surface. Modelled $\gamma_{NO_2 \rightarrow HONO}$ was calculated using Eq. 6 and Eq. 7 with a constant surface area of 1.6×10^{-2} m^2m^{-3} chosen to match the aerosol surface area density of $(1.6 \pm 0.8) \times 10^{-2}$ m^2m^{-3} shown in the experimental [HONO] values in (a).

26

548 In previous work that investigated HONO production from humic acid aerosols, a saturation
549 effect was seen with HONO production plateauing with increasing NO_2 mixing ratio (Stemmler
550 et al., 2007), with the decreasing uptake coefficient, $\gamma_{NO_2 \rightarrow HONO}$, with increasing NO_2 being
551 attributed to NO_2 fully saturating available surface sites. However, the observed decrease of
552 [HONO] at the high NO_2 mixing ratios shown in Figure 8 and Figure 10a suggests that
553 additional reactions on the surface may remove HONO and result in the reduction of [HONO]
554 that is measured. As [HONO] decreases with the increase in the NO_2 mixing ratio, the removal
555 process should either involve NO_2 directly:

$$HONO + NO_2 \rightarrow NO + HNO_3 \tag{R19}$$
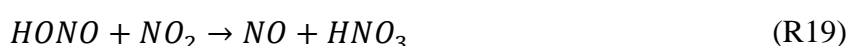
556 or involve species made rapidly from NO_2 on the surface, such as NO_2^+:

$$HONO_{(ads)} + NO_2^+{}_{(ads)} \rightarrow H^+ + 2NO + O_2 \tag{R19a}$$
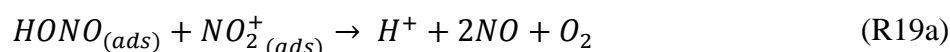
557 which may be present at high enough concentrations of HNO_3 on the surface (Syomin and
558 Finlayson-Pitts, 2003) or following reaction with h_{VB}^+, or a product of the reaction of
559 $O_2^- (or\ e_{CB}^-)$ with NO_2 (R4) i.e. NO_2^-. Similar results were observed in a study by El Zein and
560 Bedjanian (2012a) where NO_2 and NO were found to be formed from the heterogeneous
561 reaction of HONO with TiO_2 surfaces in both dark and illuminated conditions suggesting the
562 loss of HONO via an auto-ionisation reaction between the gas phase and adsorbed HONO to
563 generate NO^+ and NO_2^- (El Zein and Bedjanian, 2012a). Additional HONO surface loss
564 pathways were assumed to occur under illuminated conditions due to the presence of e^- and h^+
565 leading to the oxidation of HONO to NO_2 and the reduction of HONO to NO (El Zein et al.,
566 2013). Transition state theory (TST) studies of the gas-phase reaction of HONO with NO_2 to
567 form HNO_3 calculated a large activation energy which varied depending on whether the
568 reaction occurs via O abstraction by HONO (159 kJ mol^{-1}) or via OH abstraction via NO_2
569 (~133-246 kJ mol^{-1})(Lu et al., 2000). In the gas-phase these reactions are too slow to be
570 important but they could be enhanced on the surface, potentially more so on a photoactive
571 surface such as TiO_2. For models 2 and 3 the shape of the trend in HONO concentration and
572 uptake coefficient, γ, versus NO_2 concentration depended strongly on the value of k_{R19} reaction,
573 R19, and the choice of a 2:1 stoichiometric ratio of the NO_2 molecules adsorbed to the HONO
574 molecules produced. Without these two key processes being included, a maximum in either the
575 HONO concentration or γ as the NO_2 concentration is increased could not be obtained in the
576 model. A third key condition was the requirement that the desorption rate coefficient, k_{R16}, be

577　larger than the rate coefficient for the loss of HONO, k_{R17} and $k_{R18}=1 \times 10^{-3}$ s^{-1}, but slower than

578　the adsorption rate coefficient, k_{R9}. Changing the values of all other kinetic parameters in the

579　model had an effect on the absolute concentration of HONO, but crucially not on the shape of

580　the trends in HONO or the uptake coefficient versus NO_2 concentration. Changing the values

581　of the rate coefficients for the gas phase loss reactions, R23-27, only had a very small impact

582　on the HONO concentration. The addition of an NO_2 dependent loss reaction to both Model 2

583　and 3 had the most significant effect on the trend in modelled HONO concentration. Though it

584　is also possible that a secondary product could remain adsorbed and therefore block active sites

585　on the TiO_2 surface, effectively poisoning the photo-catalyst, NO_2 independent loss reactions

586　in the model, k_{R17} and k_{R18} had little effect on the trend in [HONO] vs NO_2, only having an

587　effect on the overall [HONO]. HNO_3 has however been shown to remain adsorbed to surfaces

588　once formed (Sakamaki et al., 1983;Pitts et al., 1984;Finlayson-Pitts et al., 2003;Ramazan et

589　al., 2004) and may also react with adsorbed HONO, further reducing the product yield

590　(Finlayson-Pitts et al., 2003): these NO_2 independent loss reactions may therefore become more

591　important at higher NO_2 concentrations and hence surface concentrations of HONO and HNO_3:

$$HONO_{(ads)} + HNO_{3(ads)} \rightarrow 2NO_{(g)} + H_2O_{(ads)} + O_{2(g)} \qquad (R17)$$
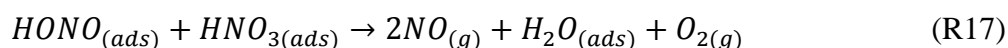
592　The photolysis of particulate nitrate was not considered in Models 2 or 3, due to the lack of

593　particulate nitrate in the system at $t=0$. The gas-to-particle conversion of any HNO_3 formed

594　was not considered to be important due to the assumption that most HNO_3 formed would

595　remain adsorbed to the aerosol surface (Sakamaki et al., 1983;Pitts et al., 1984;Finlayson-Pitts

596　et al., 2003;Ramazan et al., 2004).

597　For Model 2, which includes the production of HONO via the Eley-Rideal mechanism, in order

598　to reproduce the experimentally observed sharp increase followed by a decrease in both

599　[HONO] and $\gamma_{NO_2 \rightarrow HONO}$ as a function of increasing NO_2 mixing ratio, the modelled rate

600　coefficient for the adsorption of a gas-phase NO_2 molecule to another the surface adsorbed

601　NO_2 to initially form the symmetric N_2O_4 dimer, k_{R12}, had to be larger than for the isomerisation

602　step to form HONO and HNO_3 via *trans*-ONO-NO$_2$, k_{R13}. Interestingly, for HONO production

603　via the Langmuir-Hinshelwood mechanism, Model 3, the modelled rate coefficient for the

604　diffusion of one NO_2 molecule across the surface to form the dimer with another NO_2 molecule,

605　k_{R14}, had to be smaller than for the isomerisation step, k_{R15}, to more closely represent the

606　experimental results for the uptake coefficient. Additionally, in order to reproduce the

607　experimental trend in HONO formation as a function of NO_2 mixing ratio, the rate coefficient

608   for the NO_2 dependent loss reaction, k_{R19}, had to be larger than the NO_2 independent reactions,

609   k_{R17} and k_{R18}, leading to $k_{R19} = 5 \times 10^{-3}$ s^{-1}. The modelled HONO concentration also sensitive

610   to the active site surface concentration: Model 3 required an active site surface concentration

611   2.5 times that of Model 2 to reproduce the peak in [HONO] at ~ 51 ppb NO_2 observed in the

612   experimental results. The reason for this is due to the difference in active site occupation in the

613   2 models: one active site is being occupied by two NO_2 molecules per HONO formed in Model

614   2 as opposed to Model 3 where two active sites are occupied per HONO formed. Regardless

615   of the choice of an Eley Rideal or Langmuir Hinshelwood mechanism, both models reproduce

616   the general shape of [HONO] and $\gamma_{NO_2 \rightarrow HONO}$ with NO_2, providing evidence that two NO_2

617   molecules are required to form HONO.

3.4   HONO production from illumination of a mixed NH_4NO_3/TiO_2 aerosol in the absence of NO_2

620   The photolysis of particulate nitrate has been postulated as a source of HONO under ambient

621   sunlit conditions during several field campaigns, from both aircraft and ground based

622   measurements (Reed et al., 2017;Ye et al., 2017a;Ye et al., 2017b). Here, experiments were

623   carried out to investigate the formation of HONO from particulate nitrate photolysis, with and

624   without the addition of a photo-catalyst. This is of significant interest for marine environments

625   downwind of arid desert regions due to the availability of TiO_2 or other photocatalytic materials

626   within aerosols in dust plumes that are transported from these regions (Hanisch and Crowley,

627   2003).

628   Using the aerosol flow tube setup described in Sections 2.1-2.4, an aqueous solution of

629   ammonium nitrate (5 g NH_4NO_3 in 500 ml milli-Q water) was used to generate nitrate aerosols.

630   At the RH used in this experiment, ~ 50 %, the aerosols were still deliquesced. For these

631   experiments the residence time of the aerosols in the illuminated region of the flow tube was

632   30 seconds (flow rate ~ 6 lpm), with the production of HONO following illumination measured

633   as a function of aerosol surface area density. The number of lamps was increased from 1 to 4,

634   increasing the photon flux from $(1.63 \pm 0.09) \times 10^{16}$ to $(8.21 \pm 2.39) \times 10^{16}$ photons cm^{-2} s^{-1}

635   and $j(NO_2)$ from $(6.43 \pm 0.30) \times 10^{-3}$ to $(3.23 \pm 0.92) \times 10^{-2}$ s^{-1}. The $j(NO_2)$, $j(HONO)$ and flux

636   values for 4 lamps were more than 4 times that of 1 lamp only due to the lamp casings being

637   mirrored, and so with 4 lamps, with 2 lamps on either side of the flow tube, the casings reflected

638   the light back into the flow tube, increasing the effective light intensity. For these experiments,

639   no gaseous NO_2 was added to the gas entering the flow tube. As shown in Figure 11, for the

640 illumination of pure nitrate aerosols, although a small amount of HONO was observed at higher

641 aerosol loadings, no statistically significant production of HONO was seen.
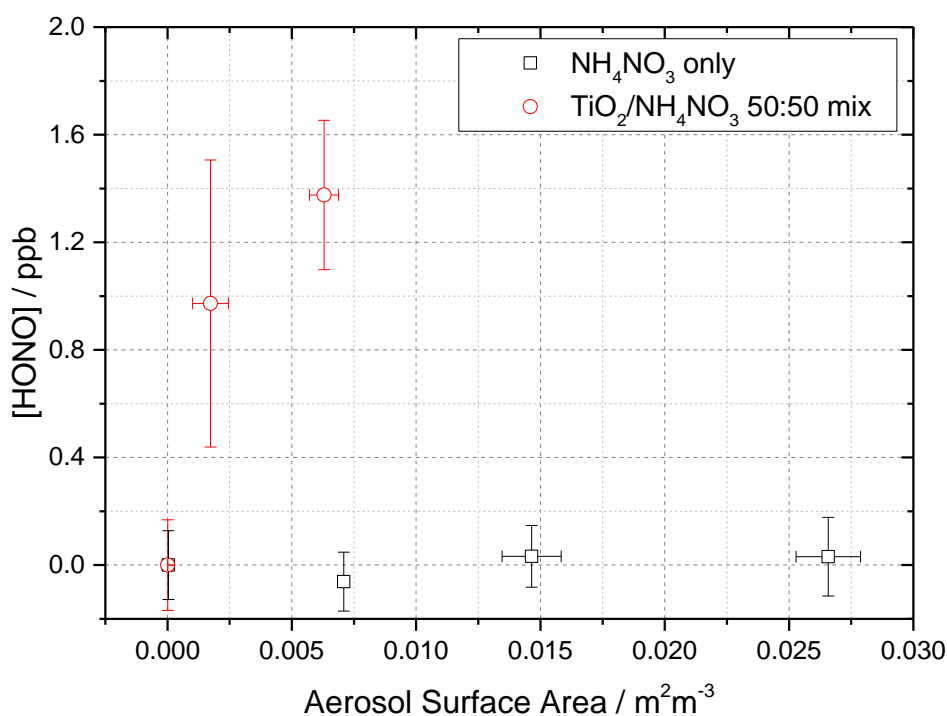

Figure 11. Dependence of the HONO concentration generated as a function of aerosol surface area density for pure NH_4NO_3 aerosol (black open squares, error bars represent 1σ) and 1:1 TiO_2/NH_4NO_3 mixed aerosol (red open circles, error bars represent 1σ). Both experiments were performed in N_2 at 295 K, an illuminated residence time of 30 s, and a lamp photon flux of $(8.29 \pm 2.39) \times 10^{16}$ photons cm^{-2} s^{-1}. The NH_4NO_3 only experiment was performed at ~50 ± 5 % RH while the TiO_2/NH_4NO_3 mix experiment was performed at 20 ± 2 % RH. For all points, the background HONO seen observed without illumination has been subtracted. At zero aerosol surface area density there is no HONO generated from the walls of the flow tube.

642 A second set of experiments were performed with an aqueous solution of titanium dioxide and

643 ammonium nitrate combined in a 1:1 mass ratio to give a TiO_2/NH_4NO_3 aerosol mixture (5 g

644 NH_4NO_3 and 5 g TiO_2 in 500 ml milli-Q water) to investigate if the photo-catalytic properties

645 of TiO_2 facilitate the production of HONO in the presence of nitrate. The RH was decreased to

646 ensure the maximum TiO_2 photocatalytic activity (Jeong et al., 2013). A recent study using

647 Raman micro spectroscopy to observe phase changes in salt particles reported an efflorescence

648 point of pure ammonium nitrate to be between 13.7-23.9 % RH (Wu et al., 2019). It is possible

649 therefore that at the RH used in this experiment, ~ 20 %, the aerosols were still deliquesced.

650 As shown in Figure 11, the presence of TiO_2 in the aerosol mixture showed a significant

651 production of HONO without the presence of NO_2, a potentially significant result for the

652 production of HONO in low NO_x environments in the presence of mixed dust/nitrate aerosols,

653   for example in oceanic regions off the coast of West Africa, or in continental regions impacted

654   by outflow from the Gobi desert. Using the Aerosol Inorganic Model (AIM) (Clegg et al.,

655   1998;Wexler and Clegg, 2002), the nitrate content of the aerosol at both 20 and 50 % RH was

656   calculated, in accordance with the experimental RH conditions. From this and the aerosol

657   volume distribution given by the SMPS, the $[NO_3^-]$ within the aerosols could be calculated.

658   The formation of HONO by photolysis of particulate nitrate is given by:

$$\frac{d[\text{HONO}]}{dt} = j(\text{pNO}_3)[\text{NO}_3^-] \tag{10}$$

659   and hence:

$$[\text{HONO}] = j(\text{pNO}_3)[\text{NO}_3^-]t \tag{11}$$

660   where $j(\text{pNO}_3)$ is the photolysis frequency of nitrate for the lamps used in these experiments

661   and t is the illumination time of the experiment. With knowledge of [HONO], $[NO_3^-]$ and $t =$

662   30 s, $j(\text{pNO}_3)$ can be calculated from a measurement of [HONO] as a function of $[NO_3^-]$, as

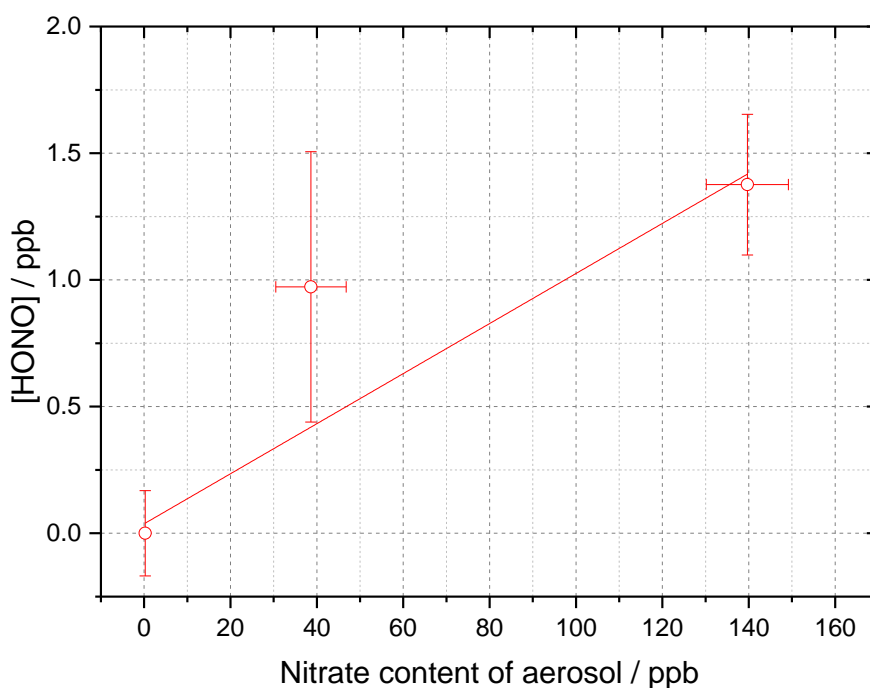663   shown in Figure 12, for the mixed nitrate/ TiO_2 experiment.

Figure 12. Dependence of [HONO] on the calculated nitrate concentration in the aerosol (using the AIM model) for the mixed TiO_2/ammonium nitrate aerosol experiment. Using equation 10 and for $t = 30$ s, the gradient gives $j(pNO_3) = (3.29 \pm 0.89) \times 10^{-4}$ s^{-1}. Experiment performed at 15 ± 1 % RH, in N_2 at 295 K with a lamp photon flux of $(8.29 \pm 2.39) \times 10^{16}$ photons cm^{-2} s^{-1}. For all points, the background HONO seen observed without illumination has been subtracted.

664   When using the 4 lamps together, the experimental particulate nitrate photolysis rate, $j(pNO_3)$,

665   was determined to be $(3.29 \pm 0.89) \times 10^{-4}$ s^{-1} for the mixed nitrate/TiO_2 aerosol. From this, it

666   is possible to estimate $j(pNO_3)$ for ambient conditions typical of the tropical marine boundary

667   layer. Taking the ratio of the experimental $j(HONO)$ for 4 lamps $((8.35 \pm 0.18) \times 10^{-3}$ s$^{-1})$ and

668   the measured $j(HONO)$ from the RHaMBLe campaign held at the Cape Verde Atmospheric

669   Observatory [May-June,2007] $(1.2 \times 10^{-3}$ s$^{-1})$ (Carpenter et al., 2010;Whalley et al., 2010;Reed

670   et al., 2017) and assuming that $j(pNO_3)$ and $j(HONO)$ scale in the same way, ambient $j(pNO_3)$

671   can be determined from:

$$j(pNO_3)_N = j(pNO_3) \times \frac{1.2 \times 10^{-3}}{j(HONO)} \qquad (12)$$

672   where $j(pNO_3)_N$ is the photolysis rate coefficient of particulate nitrate at Cape Verde, $j(pNO_3)$

673   is the experimentally determined photolysis rate coefficient of particulate nitrate to form

674   HONO and $j(HONO)$ is the HONO photolysis rate coefficient calculated from the

675   experimentally determined $j(NO_2)$.

676   Using $j(pNO_3) = (3.29 \pm 0.89) \times 10^{-4}$ s^{-1}, the rate of HONO production from nitrate photolysis

677   at Cape Verde was calculated to be $j(pNO_3)_N = (4.73 \pm 1.01) \times 10^{-5}$ s^{-1} from the mixed

678   nitrate/TiO_2 aerosol experiment. Although for pure nitrate aerosol in the absence of TiO_2 the

679   data were scattered and the HONO production small (Figure 11), an upper limit estimate of

680    $j(pNO_3)_N = (1.06 \pm 1.15) \times 10^{-6}$ s^{-1} under conditions at Cape Verde could be made using

681   equation 11**(11)**, as done for rate of HONO production from mixed nitrate/TiO_2 aerosols. The

682   atmospheric implications of this will be considered below.

683   4   Implications of HONO production from TiO_2 for tropospheric chemistry

684   4.1   Production of HONO from sunlight aerosols containing TiO_2 in the
685   presence of NO_2

686   For the reactive uptake of NO_2 onto illuminated TiO_2 particles as a function of the initial NO_2

687   mixing ratio, as shown in Figure 8, a maximum value of $\gamma_{NO_2 \rightarrow HONO} = (1.26 \pm 0.17) \times 10^{-4}$

688 was determined at 51 ± 5 ppb NO_2 for a photon flux from the lamp of $(1.63 ± 0.09) \times 10^{16}$
689 photons cm^{-2} s^{-1}. These experiments were for single-component TiO_2 particles, and so for dust
690 aerosols a value of $\gamma_{NO_2 \to HONO} = (1.26 ± 0.17) \times 10^{-5}$ is appropriate assuming a 10 % fraction
691 of TiO_2 and/or other photoactive materials (which behave similarly for HONO production) in
692 mineral dust (Hanisch and Crowley, 2003). Dust aerosols are transported from the Gobi desert
693 to urban areas of China where high NO_x and nitrate aerosol concentrations have been observed
694 and in these areas HONO production facilitated by photo-catalysts may be important (Saliba
695 et al., 2014).

696 Using an average daytime maximum for $[NO_2]$, $j(NO_2)$ and aerosol surface area measurements
697 for a non-haze period in May-June in 2018 in Beijing, of 50 ppb, 1×10^{-2} s^{-1} and 2.5×10^{-3} m^2
698 m^{-3} (of which a maximum of 0.3 % was assumed to be TiO_2, though this could be higher in
699 dust impacted events (Schleicher et al., 2010)) respectively, a production rate of HONO of 1.70
700 $\times 10^5$ molecules cm^{-3} s^{-1} (~24.8 ppt h^{-1}) has been estimated using the maximum reactive uptake
701 coefficient measured in this work, $\gamma_{NO_2 \to HONO} = (1.26 ± 0.17) \times 10^{-4}$. The average RH in
702 Beijing during summertime is significantly higher than the range of RH used in the TiO_2
703 aerosol experiments. In previous work (Gustafsson et al., 2006), the NO_2 reactive uptake
704 coefficient decreased for relative humidities above those studied here, and hence the HONO
705 production calculated under the conditions in Beijing may represent an upper limit. The lamp
706 used to illuminate the TiO_2 aerosols in these experiments gives rise to $j(NO_2) = (6.43 ± 0.3) \times$
707 10^{-3} s^{-1}, and so $\gamma_{NO_2 \to HONO}$ has been scaled by a factor of 1.55 to match the noon $j(NO_2)$
708 measured in May-June 2018 in Beijing (10^{-2} s^{-1}), to take into account the relatively small
709 difference in experimental and atmospheric photon flux for Beijing. The HONO production
710 rate estimated here for noontime summer [May-June 2018] in Beijing (~25 ppt hr^{-1}) is similar
711 to the value for the maximum production of HONO from urban humic acid aerosol surfaces in
712 Europe, 17 ppt h^{-1} at 20 ppb NO_2 reported by Stemmler et al., 2007. For comparison, the net
713 gaseous production rate of HONO at noon in May-June 2018 Beijing was determined from the
714 measured rate of gas-phase production and losses:

$$P_{HONO} = k_{OH+NO}[OH][NO] - (j(HONO) \times [HONO] + k_{OH+HONO}[OH][HONO]) \quad (13)$$

715 where $k_{OH+NO} = 3.3 \times 10^{-11}$ cm^3 $molecule^{-1}$ s^{-1} (Atkinson et al., 2004), $k_{OH+HONO} = 6 \times 10^{-12}$
716 cm^3 $molecule^{-1}$ s^{-1} (Atkinson et al., 2004) and $j(HONO)=1 \times 10^{-2}$ s^{-1} for an average maximum
717 noontime OH concentration of 8×10^6 molecules cm^{-3} (Whalley et al., 2020), NO

718   concentration of 1.45 ppb (Whalley et al., 2020) and HONO concentration of 0.8 ppb (Whalley

719   et al., 2020).

720   The net gas-phase production of HONO from equation 13 was calculated to be -3.8 ppb hr^{-1} (a

721   net loss) as expected due to HONO loss by photolysis peaking at solar noon, suggesting the

722   production of HONO heterogeneously from TiO_2 and NO_2 (~25 ppt hr^{-1}) would have little

723   effect on the overall HONO budget for Beijing summertime at noon.

4.2 Production of HONO from photolysis of mixed dust/nitrate aerosols

725   Oceanic environments, for example the Atlantic Ocean which is impacted by both dust aerosols

726   from the Sahara and high concentrations of mixed nitrate aerosols from sea spray, and despite

727   low NO_2 concentrations could be important for particulate nitrate photolysis as a source of

728   HONO (Hanisch and Crowley, 2003;Ye et al., 2017b). From the particulate nitrate photolysis

729   experiments in the absence of NO_2 conducted here, a $j(pNO_3)_N$= (4.73 ± 1.01) × 10^{-5} s^{-1} was

730   determined in the presence of the TiO_2 photo-catalysts (Section 3.4). Using the experimental

731    $j(pNO_3)$, scaled to typical ambient light levels, and a mean noon concentration of nitrate

732   aerosols of 400 ppt measured at Cape Verde (Reed et al., 2017), taken as an example marine

733   boundary layer environment with a high concentration of mineral dust aerosols, a rate of

734   HONO production from particulate nitrate at Cape Verde was calculated as 4.65 × 10^5

735   molecule cm^{-3} s^{-1} (68 ppt hr^{-1}). We note that this value would be ~ 50 times smaller for pure

736   nitrate aerosols. The missing rate of HONO production i.e. not taken into account by the gas

737   phase production and loss, P_{other}, from the Cape Verde RHaMBLe campaign, can be calculated

738   using the observed HONO concentration, [HONO] and the known gas-phase routes for HONO

739   production and loss:

$$P_{other} = ([\text{HONO}](j(\text{HONO}) + k_{OH+HONO}[\text{OH}])) - (k_{OH+NO}[\text{OH}][\text{NO}]) \qquad (14)$$

740   where k_{OH+NO} = 3.3 × 10^{-11} cm^3 molecule^{-1} s^{-1} (Atkinson et al., 2004), $k_{OH+HONO}$ = 6 × 10^{-12}

741   cm^3 molecule^{-1} s^{-1} (Atkinson et al., 2004) and $j(\text{HONO})$=2 × 10^{-3} s^{-1} for average maximum

742   measured concentrations of 1 × 10^7 molecules cm^{-3} for OH (Whalley et al., 2010), 5.41 × 10^7

743   molecule cm^{-3} for NO (Whalley et al., 2010) and 1.23 × 10^8 molecule cm^{-3} for HONO (Whalley

744   et al., 2010).

745   Using equation 14 this missing HONO production rate for Cape Verde was 34.6 ppt hr^{-1}, which

746   is within a factor of two of the rate of HONO production (68 ppt hr-1) calculated from nitrate

747   photolysis using our experimental HONO production data for mixed nitrate/TiO_2 aerosols.

748 These results provide further evidence that particulate nitrate photolysis in the presence of
749 photocatalytic compounds such as TiO_2 found in dust could be significant in closing the HONO
750 budget for this environment (Whalley et al., 2010;Reed et al., 2017;Ye et al., 2017a).

5 Conclusions.

752 The experimental production of HONO from both illuminated TiO_2 aerosols in the presence of
753 NO_2 and from mixed nitrate/TiO_2 aerosols in the absence of NO_2 was observed, with the
754 HONO concentrations measured using photo-fragmentation laser-induced fluorescence
755 spectroscopy. Using experimental data, the reactive uptake of NO_2 onto the TiO_2 aerosol
756 surface to produce HONO, $\gamma_{NO_2 \rightarrow HONO}$, was determined for NO_2 mixing ratios ranging from
757 34 to 400 ppb, with a maximum $\gamma_{NO_2 \rightarrow HONO}$ value of $(1.26 \pm 0.17) \times 10^{-4}$ for single-component
758 TiO_2 aerosols observed at 51 ppb NO_2, and for a lamp photon flux of $(1.65 \pm 0.02) \times 10^{16}$
759 photons cm^{-2} s^{-1} (integrated between 290 and 400 nm). The measured reactive uptake
760 coefficient, $\gamma_{NO_2 \rightarrow HONO}$, showed an increase then subsequent decrease as a function of NO_2
761 mixing ratio, peaking at 51 ± 5 ppb. Box modelling studies supported a mechanism involving
762 two NO_2 molecules on the aerosol surface per HONO molecule generated, providing evidence
763 for the formation of a surface-bound NO_2 dimer intermediate. The exact mechanism for HONO
764 formation, for examples the step(s) which are accelerated in the presence of light, remains
765 unclear, although previous studies would suggest the process occurs via the isomerisation of
766 the symmetric N_2O_4 dimer to give *trans*-ONO-NO_2, either via *cis*-ONO-NO_2 or directly,
767 suggested to be more reactive with water than the symmetric dimer (Finlayson-Pitts et al.,
768 2003;Ramazan et al., 2004;Ramazan et al., 2006;de Jesus Madeiros and Pimentel, 2011;Liu
769 and Goddard, 2012;Murdachaew et al., 2013;Varner et al., 2014). Investigations into the RH
770 dependence of the HONO production mechanism on TiO_2 aerosols showed a peak in
771 production between ~25-30 % RH, with lower HONO production at higher NO_2 mixing ratios
772 observed for all RHs tested. The increase in HONO production with increasing RH can be
773 attributed to a higher concentration of H_2O on the surface increasing its availability for the
774 hydrolysis reaction to give HONO, whereas a decrease in HONO production after RH ~ 30 %
775 could be due to the increased water surface concentration inhibiting the adsorption of NO_2.
776 Using the laboratory reactive uptake coefficient for HONO production, $\gamma_{NO_2 \rightarrow HONO}$, the rate of
777 production of HONO from illuminated aerosols in Beijing in summer for typical NO_2 mixing
778 ratios and aerosol surface areas was found to be similar to that estimated previously for the
779 production of HONO from urban humic acid aerosol surfaces in Europe.

In the absence of NO_2, significant HONO production from 50:50 mixed nitrate/TiO_2 aerosols was measured. Using the experimental HONO concentrations observed, a rate of HONO production from nitrate photolysis was calculated, which was then scaled to the ambient conditions encountered at the Cape Verde Atmospheric Observatory in the tropical marine boundary layer. A HONO production rate of 68 ppt hr^{-1} for the mixed nitrate/TiO_2 aerosol was found for CVAO conditions, similar in magnitude to the missing HONO production rate that had been calculated previously in order to bring modelled HONO concentrations into line with field-measured values at CVAO. These results provide further evidence that aerosol particulate nitrate photolysis may be significant as a source of HONO, and hence NO_x, in the remote marine boundary layer, where mixed aerosols containing nitrate and a photo-catalytic species such as TiO_2, as found in dust, are present.

However, the production of HONO from pure, deliquesced ammonium nitrate aerosols alone could not be definitively confirmed over the range of conditions used in our experiments, suggesting that another component within the aerosol is necessary for HONO production. Future work should be directed towards studying pure nitrate aerosols over a wider range of conditions, for example varying the aerosol pH, and also adding other chemical species into the aerosol which may promote HONO production.

References

Alicke, B., Platt, U., and Stutz, J.: Impact of nitrous acid photolysis on the total hydroxyl radical budget during the Limitation of Oxidant Production/Pianura Padana Produzione di Ozono study in Milan, J. Geophys. Res. Atmos., 107, https://doi.org/10.1029/2000JD000075, 2002.

Atkinson, R., Baulch, D. L., Cox, R. A., Crowley, J. N., Hampson, R. F., Hynes, R. G., Jenkin, M. E., Rossi, M. J., and Troe, J.: Evaluated kinetic and photochemical data for atmospheric chemistry: Volume I - gas phase reactions of O_x, HO_x, NO_x and SO_x species, Atmos. Chem. Phys., 4, 1461-1738, https://doi.org/10.5194/acp-4-1461-2004, 2004.

Beckers, H., Zeng, X., and Willner, H.: Intermediates involved in the oxidation of nitrogen monoxide: Photochemistry of the cis-$N_2O_2 \cdot O_2$ complex and of sym-N_2O_4 in Solid Ne Matrices,

Chemistry–A European Journal, 16, 1506-1520, https://doi.org/10.1002/chem.200902406, 2010.

Bedjanian, Y., and El Zein, A.: Interaction of NO_2 with TiO_2 Surface Under UV Irradiation: Products Study, J. Phys. Chem. A, 116, 1758-1764, https://doi.org/10.1021/jp210078b, 2012.

Boustead, G. A.: Measurement of nitrous acid production from aerosol surfaces using Photo-Fragmentation Laser-Induced Fluorescence, School of Chemistry, University of Leeds, 2019.

Bröske, R., Kleffmann, J., and Wiesen, P.: Heterogeneous conversion of NO_2 on secondary organic aerosol surfaces: A possible source of nitrous acid (HONO) in the atmosphere?, Atmos. Chem. Phys., 3, 469-474, https://doi.org/10.5194/acp-3-469-2003, 2003.

Cantrell, C., Zimmer, A., and Tyndall, G. S.: Adsorption cross sections for water vapor from 183 to 193 nm, Geophys. Res. Lett., 24, 2195-2198, https://doi.org/10.1029/97GL02100, 1997.

Carpenter, L. J., Fleming, Z. L., Read, K. A., Lee, J. D., Moller, S. J., Hopkins, J. R., Purvis, R. M., Lewis, A. C., Müller, K., Heinold, B., Herrmann, H., Fomba, K. W., van Pinxteren, D., Müller, C., Tegen, I., Wiedensohler, A., Müller, T., Niedermeier, N., Achterberg, E. P., Patey, M. D., Kozlova, E. A., Heimann, M., Heard, D. E., Plane, J. M. C., Mahajan, A., Oetjen, H., Ingham, T., Stone, D., Whalley, L. K., Evans, M. J., Pilling, M. J., Leigh, R. J., Monks, P. S., Karunaharan, A., Vaughan, S., Arnold, S. R., Tschritter, J., Pöhler, D., Frieß, U., Holla, R., Mendes, L. M., Lopez, H., Faria, B., Manning, A. J., and Wallace, D. W. R.: Seasonal characteristics of tropical marine boundary layer air measured at the Cape Verde Atmospheric Observatory, Journal of Atmospheric Chemistry, 67, 87-140, https://doi.org/10.1007/s10874-011-9206-1, 2010.

Chen, H., Nanayakkara, C. E., and Grassian, V. H.: Titanium dioxide photocatalysis in atmospheric chemistry, Chem. Rev., 112, 5919-5948, https://doi.org/10.1021/cr3002092, 2012.

Clegg, S. L., Brimblecombe, P., and Wexler, A. S.: Thermodynamic model of the system $H^+-NH_4^+- Na^+- SO_4^{2-} NO_3^-- Cl^- H_2O$ at 298.15 K, J. Phys. Chem. A, 102, 2155-2171, https://doi.org/10.1021/jp973043j, 1998.

Crilley, L. R., Kramer, L. J., Ouyang, B., Duan, J., Zhang, W., Tong, S., Ge, M., Tang, K., Qin, M., Xie, P., Shaw, M. D., Lewis, A. C., Mehra, A., Bannan, T. J., Worrall, S. D., Priestley, M., Bacak, A., Coe, H., Allan, J., Percival, C. J., Popoola, O. A. M., Jones, R. L., and Bloss, W. J.: Intercomparison of nitrous acid (HONO) measurement techniques in a megacity (Beijing), Atmos. Meas. Tech., 12, 6449-6463, https://doi.org/10.5194/amt-12-6449-2019, 2019.

de Jesus Madeiros, D., and Pimentel, A. S.: New insights in the atmospheric HONO formation: new pathways for N_2O_4 isomerisaton and NO_2 dimerisation in the presence of water. , J. Phys. Chem. A, 115, 6357-6365, https://doi.org/10.1021/jp1123585, 2011.

Dupart, Y., Fine, L., D'Anna, B., and George, C.: Heterogeneous uptake of NO_2 on Arizona Test Dust under UV-A irradiation: an aerosol flow tube study, Aeolian Res., 15, 45-51, https://doi.org/10.1016/j.aeolia.2013.10.001, 2014.

El Zein, A., and Bedjanian, Y.: Reactive Uptake of HONO to TiO_2 Surface: "Dark" Reaction, J. Phys. Chem. A, 116, 3665-3672, https://doi.org/10.1021/jp300859w, 2012a.

El Zein, A., and Bedjanian, Y.: Interaction of NO_2 with TiO_2 surface under UV irradiation: measurements of uptake coefficient, Atmos. Chem. Phys., 12, 1013-1020, https://doi.org/10.5194/acp-12-1013-2012, 2012b.

El Zein, A., Bedjanian, Y., and Romanias, M. N.: Kinetics and products of HONO interaction with TiO_2 surface under UV irradiation, Atmos. Environ., 67, 203-210, https://doi.org/10.1016/j.atmosenv.2012.11.016, 2013.

Fateley, W. G., Bent, H. A., and Crawford Jr, B.: Infrared spectra of the frozen oxides of nitrogen, J. Chem. Phys., 31, 204-217, https://doi.org/10.1063/1.1730296, 1959.

Finlayson-Pitts, B. J., Wingen, L. M., Summer, A. L., Syomin, D., and Ramazan, K. A.: The heterogeneous hydrolysis of NO_2 in laboratory systems in outdoor and indoor atmospheres: An intergrated mechanism, Phys.Chem.Phys.Chem, 5, 223-242, https://doi.org/10.1039/b208564j, 2003.

Forney, D., Thompson, W. E., and Jacox, M. E.: The vibrational spectra of molecular ions isolated in solid neon. XI. NO_2^+ , NO_2^-, and NO_3^-, The Journal of Chemical Physics, 99, 7393-7403, https://doi.org/10.1063/1.465720, 1993.

Gandolfo, A., Bartolomei, V., Gomez Alvarez, E., Tlili, S., Gligorovski, S., Kleffmann, J., and Wortham, H.: The effectiveness of indoor photocatalytic paints on NOx and HONO levels, Applied Catalysis B: Environmental, 166-167, 84-90, https://doi.org/10.1016/j.apcatb.2014.11.011, 2015.

Gandolfo, A., Rouyer, L., Wortham, H., and Gligorovski, S.: The influence of wall temperature on NO2 removal and HONO levels released by indoor photocatalytic paints, Applied Catalysis B: Environmental, 209, 429-436, https://doi.org/10.1016/j.apcatb.2017.03.021, 2017.

George, C., Strekowski, R. S., Kleffmann, J., Stemmler, K., and Ammann, M.: Photoenhanced uptake of gaseous NO_2 on solid organic compounds: a photochemical source of HONO?, Faraday Discuss., 130, https://doi.org/10.1039/b417888m, 2005.

George, I. J., Matthews, P. S. J., Whalley, L. K., Brooks, B., Goddard, A., Baeza-Romero, M., and Heard, D. E.: Measurements of uptake coefficients for heterogeneous loss of HO_2 onto submicron inorganic salt aerosols., Phys. Chem. Chem. Phys., 15, 12829-12845, https://doi.org/10.1039/c3cp51831k, 2013.

Ginoux, P., Chin, M., Tegen, I., Prospero, J. M., Holben, B., Dubovik, O., and Lin, S. J.: Sources and distributions of dust aerosols simulated with the GOCART model, J. Geophys. Res. Atmos., 106, 20255-20273, https://doi.org/10.1029/2000JD000053, 2001.

Givan, A., and Loewenschuss, A.: Fourier transform infrared and Raman studies on solid nitrogen dioxide: Temperature cycling of ordered, disordered, and multicomponent layers, The Journal of Chemical Physics, 90, 6135-6142, https://doi.org/10.1063/1.456379, 1989a.

Givan, A., and Loewenschuss, A.: On the intermolecularity or intramolecularity of nitrosonium nitrate formation in thin films of nitrogen dioxide: A Fourier transform infrared study, The Journal of chemical physics, 91, 5126-5127, https://doi.org/10.1063/1.457609, 1989b.

Givan, A., and Loewenschuss, A.: Fourier transform infrared study of amorphous N_2O_4 solid: Destabilization with inert impurities, The Journal of chemical physics, 94, 7562-7563, https://doi.org/10.1063/1.460192, 1991.

Goodman, A. L., Bernard, E. T., and Grassian, V. H.: Spectroscopic study of nitric acid and water adsorption on oxide particles: enhanced nitric acid uptake kinetics in the presence of adsorbed water, J. Phys. Chem. A, 105, 6443-6457, https://doi.org/10.1021/jp0037221, 2001.

Gustafsson, R. J., Orlov, A., Griffiths, P. T., Cox, R. A., and Lambert, R. M.: Reduction of NO_2 to nitrous acid on illuminated titanium dioxide aerosol surfaces: implications for

photocatalysis and atmospheric chemistry, Chem. Commun., 37, 3936-3938, https://doi.org/10.1039/b609005b, 2006.

Hanisch, F., and Crowley, J. N.: Ozone decomposition on Saharan dust: an experimental investigation, Atmos. Chem. Phys., 3, 119-130, https://doi.org/10.5194/acp-3-119-2003, 2003.

Harrison, R. M., Peak, J. D., and Collins, G. M.: Tropospheric cycle of nitrous acid, J. Geophys. Res. Atmos., 101, 14429-14439, https://doi.org/10.1029/96JD00341, 1996.

Heard, D. E.: Atmospheric field measurements of the hydroxyl radical using Laser-Induced Fluorescence spectroscopy, Annu. Rev. Phys. Chem., 57, 191-216, https://doi.org/10.1146/annurev.physchem.57.032905.104516, 2006.

Jeong, M.-G., Park, E. J., Seo, H. O., Kim, K.-D., Kim, Y. D., and Lim, D. C.: Humidity effect on photocatalytic activity of TiO_2 and regeneration of deactivated photocatalysts, Appl. Surf. Sci., 271, 164-170, https://doi.org/10.1016/j.apsusc.2013.01.155, 2013.

Kleffmann, J.: Daytime sources of nitrous acid (HONO) in the atmospheric boundary layer, Chem. Phys. Chem., 8, 1137-1144, https://doi.org/10.1002/cphc.200700016, 2007.

Kurtenbach, R., Becker, K. H., Gomes, J. A. G., Kleffmann, J., Lörzer, J. C., Spittler, M., Wiesen, P., Ackermann, R., Geyer, A., and Platt, U.: Investigations of emissions and heterogeneous formation of HONO in road traffic tunnel, Atmos. Environ., 35, 3385-3394, https://doi.org/10.1016/S1352-2310(0)00138-8, 2001.

Langridge, J. M., Gustafsson, R. J., Griffiths, P. T., Cox, R. A., Lambert, R. M., and Jones, R. L.: Solar driven nitrous acid formation on building material surfaces containing titanium dioxide: A concern for air quality in urban areas?, Atmos. Environ., 43, 5128-5131, https://doi.org/10.1016/j.atmosenv.2009.06.046, 2009.

Lee, J. D., Whalley, L. K., Heard, D. E., Stone, D., Dunmore, R. E., Hamilton, J. F., Young, D. E., Allan, J. D., Laufs, S., and Kleffmann, J.: Detailed budget analysis of HONO in central London reveals a missing daytime source, Atmos. Chem. Phys., 16, 2747-2764, https://doi.org/10.5194/acp-16-2747-2016, 2016.

Levy, H.: Normal atmosphere: large radical and formaldehyde concentrations predicted, Science, 173, 141-143, https://doi.org/10.1126/science.173.3992.141, 1971.

Li, S., Matthews, J., and Sinha, A.: Atmospheric hydroxyl radical production from electronically excited NO_2 and H_2O, Science, 319, https://doi.org/10.1126/science.1151443, 2008.

Liao, W., Hecobian, A., Mastromarino, J., and Tan, D.: Development of a photo-fragmentation/laser-induced fluorescence measurement of atmospheric nitrous acid, Atmos. Environ., 40, 17-26, https://doi.org/10.1016/j.atmosenv.2005.07.001, 2006.

Liao, W., Hecobian, A., Mastromarino, J., and Tan, D.: Development of a photo-fragmentation/laser-induced fluorescence measurement of atmospheric nitrous acid, Atmospheric Envrionment, 40, 17-26, https://doi.org/10.1016/j.atmosenv.2005.07.001, 2007.

Liu, W. G., and Goddard, W. A.: First-principle study of the role of interconversion between NO_2, N_2O_4, *cis*-ONO-NO_2, and *trans*-ONO-NO_2 in chemical processes, J. Am. Chem. Soc., 134, 12970-12978, https://doi.org/10.1021/ja300545e, 2012.

Lu, K., Fuchs, H., Hofzumahaus, A., Tan, Z., Wang, H., Zhang, L., Schmitt, S. H., Rohrer, F., Bohn, B., Broch, S., Dong, H., Gkatzelis, G. I., Hohaus, T., Holland, F., Li, X., Liu, Y., Liu, Y., Ma, X., Novelli, A., Schlag, P., Shao, M., Wu, Y., Wu, Z., Zeng, L., Hu, M., Kiendler-Scharr, A., Wahner, A., and Zhang, Y.: Fast Photochemistry in Wintertime Haze:

943 Consequences for Pollution Mitigation Strategies, Environ. Sci. Technol., 53, 10676-10684,
944 https://doi.org/10.1021/acs.est.9b02422, 2019.

945 Lu, X., Park, J., and Lin, M. C.: Gas phase reactions of HONO with NO_2, O_3 and HCl: Ab initio
946 and TST study, J. Phys. Chem. A, 104, 8730-8738, https://doi.org/10.1021/jp001610o, 2000.

947 Matthews, P. S. J., Baeza-Romero, M. T., Whalley, L. K., and Heard, D. E.: Uptake of HO_2
948 radicals onto Arizona test dust particles using an aerosol flow tube, Atmos. Chem. Phys., 14,
949 7397-7408, https://doi.org/10.5194/acp-14-7397-2014, 2014.

950 MCPA software Ltd.: Facsimile, 2020.

951 Michoud, V., Colomb, A., Borbon, A., Miet, K., Beekmann, M., Camredon, M., Aumont, B.,
952 Perrier, S., Zapf, P., Siour, G., Ait-Helal, W., Afif, C., Kukui, A., Furger, M., Dupont, J. C.,
953 Haeffelin, M., and Doussin, J. F.: Study of the unknown HONO daytime source at a European
954 suburban site during the MEGAPOLI summer and winter field campaigns, Atmos. Chem.
955 Phys., 14, 2805-2822, https://doi.org/10.5194/acp-14-2805-2014, 2014.

956 Moon, D. R., Ingham, T., Whalley, L. K., Seakins, P. W., Baeza-Romero, M. T., and Heard,
957 D. E.: Production of OH and HO_2 radicals from near-UV irradiated airborne TiO_2
958 nanoparticles, Phys.Chem.Phys.Chem, 21, 2325-2336, https://doi.org/10.1039/C8CP06889E,
959 2019.

960 Murdachaew, G., Varner, M. E., Philips, L. F., Finlayson-Pitts, B. J., and Gerber, R. B.:
961 Nitrogen dioxide at the air-water interface: trapping, adsorption, and solvation in the bulk and
962 at the surface, Phys. Chem. Chem. Phys., 15, 204-212, https://doi.org/10.1039/c2cp42810e,
963 2013.

964 Nakamura, I., Sugihara, S., and Takeuchi, K.: Mechanism for NO photooxidation over the
965 oxygen-deficient TiO_2 powder under visible light irradiation, Chem. Lett., 29, 1276-1277,
966 https://doi.org/10.1246/cl.2000.1276, 2000.

967 Ndour, M., D'Anna, B., George, C., Ka, O., Balkanski, Y., Kleffman, J., Stemmler, K., and
968 Ammann, M.: Photoenhanced uptake of NO_2 on mineral dust: Laboratory experiments and
969 model simulations, Geophys. Res. Lett., 35, L05812, https://doi.org/10.1029/2007GL032006,
970 2008.

971 Oswald, R., Behrendt, T., Ermel, M., Wu, D., Su, H., Cheng, Y., Breuninger, C., Moravek, A.,
972 Mougin, E., Delon, C., Loubet, B., Pommerening-Röser, A., Sörgel, M., Pöschl, U., Hoffmann,
973 T., Andeae, M. O., Meixner, F. X., and Trebs, I.: HONO emissions from soil bacteria as a
974 major source of atmospheric reactive nitrogen, Science, 341, 1233-1235,
975 https://doi.org/10.1126/science.1242266, 2013.

976 Pinnick, D., Agnew, S., and Swanson, B.: Fluid dinitrogen tetroxide at very high pressure and
977 high temperature: observation of the nitrite isomer, The Journal of Physical Chemistry, 96,
978 7092-7096, https://doi.org/10.1021/j100196a046, 1992.

979 Pitts, J. N., Sanhueza, E., Atkinson, R., Carter, W. P. L., Winer, A. M., Harris, G. W., and
980 Plum, C. N.: An investigation of the dark formation of nitrous acid in environmental chambers,
981 Int. J. Chem. Kinet., 16, 919-939, https://doi.org/10.1002/kin.550160712, 1984.

982 Platt, U., Perner, D., Harris, G. W., Winer, A. M., and Pitts, J. N.: Observations of nitrous acid
983 in an urban atmosphere by differential optical absorption, Nature, 285, 312-314,
984 https://doi.org/10.1038/285312a0, 1980.

985 Ramazan, K. A., Syomin, D., and Finlayson-Pitts, B. J.: The photochemical production of
986 HONO during the heterogeneous hydrolysis of NO2, Phys. Chem. Chem. Phys., 6, 3836-3843,
987 https://doi.org/10.1039/B402195A, 2004.

988 Ramazan, K. A., Wingen, L. M., Miller, Y., Chaban, G. M., Gerber, R. B., Xantheas, S. S., and
989 Finlayson-Pitts, B. J.: New experimental and theoretical approach to the heterogeneous
990 hydrolysis of NO_2: key role of molecular nitric acid and its complexes, J. Phys. Chem. A, 110,
991 6886-6897, https://doi.org/10.1021/jp056426n, 2006.

992 Reed, C., Evans, M. J., Crilley, L. R., Bloss, W. J., Sherwen, T., Read, K. A., Lee, J. D., and
993 Carpenter, L. J.: Evidence for renoxification in the tropical marine boundary layer, Atmos.
994 Chem. Phys., 17, 4081-4092, https://doi.org/10.5194/acp-17-4081-2017, 2017.

995 Sakamaki, F., Hatakeyama, S., and Akimoto, H.: Formation of nitrous acid and nitric oxide in
996 the heterogeneous dark reaction of nitrogen dioxide and water vapor in a smog chamber, Int.
997 J. Chem. Kinet., 15, 1013-1029, https://doi.org/10.1002/kin.550151006, 1983.

998 Saliba, N., Moussa, S., and Tayyar, G.: Contribution of airborne dust particles to HONO
999 sources, Atmos. Chem. Phys. Discuss., 14, https://doi.org/10.5194/acpd-14-4827-2014, 2014.

1000 Sander, S., Friedl, R., Barker, J., Golden, D., Kurylo, M., Wine, P., Abbatt, J., Burkholder, J.,
1001 Kolb, C., and Moortgat, G.: Chemical kinetics and photochemical data for use in atmospheric
1002 studies, evaluation number 14, JPL Publ., 02, 25, 2003.

1003 Schleicher, N., Norra, S., Chai, F., Chen, Y., Wang, S., and Stüben, D.: Anthropogenic versus
1004 geogenic contribution to total suspended atmospheric particulate matter and its variations
1005 during a two-year sampling period in Beijing, China, J. Environ. Monit., 12, 434-441,
1006 https://doi.org/10.1039/B914739J, 2010.

1007 Seifert, N. A., Zaleski, D. P., Fehnel, R., Goswami, M., Pate, B. H., Lehmann, K. K., Leung,
1008 H. O., Marshall, M. D., and Stanton, J. F.: The gas-phase structure of the asymmetric, trans-
1009 dinitrogen tetroxide (N_2O_4), formed by dimerization of nitrogen dioxide (NO_2), from rotational
1010 spectroscopy and ab initio quantum chemistry, The Journal of Chemical Physics, 146, 134305,
1011 https://doi.org/10.1063/1.4979182, 2017.

1012 Shan, J. H., Wategaonkar, S. J., and Vasudev, R.: Vibrational state dependence of the A state
1013 lifetime of HONO, Chem. Phys. Lett., 158, 317-320, https://doi.org/10.1016/0009-
1014 2614(89)87343-9, 1989.

1015 Slater, E. J., Whalley, L. K., Woodward-Massey, R., Ye, C., Lee, J. D., Squires, F., Hopkins,
1016 J. R., Dunmore, R. E., Shaw, M., Hamilton, J. F., Lewis, A. C., Crilley, L. R., Kramer, L.,
1017 Bloss, W., Vu, T., Sun, Y., Xu, W., Yue, S., Ren, L., Acton, W. J. F., Hewitt, C. N., Wang, X.,
1018 Fu, P., and Heard, D. E.: Elevated levels of OH observed in haze events during wintertime in
1019 central Beijing, Atmos. Chem. Phys. Discuss., 2020, 1-43, https://doi.org/10.5194/acp-2020-
1020 362, 2020.

1021 Spataro, F., and Ianniello, A.: Sources of atmospheric nitrous acid: State of the science, current
1022 research needs, and future prospects, J. Air Waste Manage. Assoc., 64, 1232-1250,
1023 https://doi.org/10.1080/10962247.2014.952846, 2014.

1024 Stemmler, K., Ndour, M., Elshorbany, Y., Kleffmann, J., D'Anna, B., George, C., Bohn, B.,
1025 and Ammann, M.: Light induced conversion of nitrogen dioxide into nitrous acid on submicron
1026 humic acid aerosol, Atmos. Chem. Phys., 7, 4237-4248, https://doi.org/10.5194/acp-7-4237-
1027 2007, 2007.

Su, H., Cheng, Y., Oswald, R., Behrendt, T., Trebs, I., Meixner, F. C., Andreae, M. O., Cheng, P., Zhang, Y., and Pöschl, U.: Soil nitrate as a source of atmospheric HONO and OH radicals, Science, 333, 1616-1618, https://doi.org/10.1126/science.1207687, 2011.

Syomin, D. A., and Finlayson-Pitts, B. J.: HONO decomposition on borosilicate glass surfaces: implications for environmental chamber studies and field experiments, Phys. Chem. Chem. Phys., 5, 5236-5242, https://doi.org/10.1039/b309851f, 2003.

Takeuchi, M., Sakamoto, K., Martra, G., Coluccia, S., and Anpo, M.: Mechanism of photoinduced superhydrophilicity on the TiO_2 photocatalyst surface, J. Phys. Chem. B, 109, 15422-15428, https://doi.org/10.1021/jp058075i, 2005.

Varner, M. E., Finlayson-Pitts, B. J., and Gerber, R. B.: Reaction of a charge-separated $ONONO_2$ species with water in the formation of HONO: an MP2 molecular dynamics study, Phys. Chem. Chem. Phys., 16, 4483-4487, https://doi.org/10.1039/c3cp55024a, 2014.

Wang, C., Bottorff, B., Reidy, E., Rosales, C. M. F., Collins, D. B., Novoselac, A., Farmer, D. K., Vance, M. E., Stevens, P. S., and Abbatt, J. P. D.: Cooking, Bleach Cleaning, and Air Conditioning Strongly Impact Levels of HONO in a House, Environ. Sci. Technol., 54, 13488-13497, 10.1021/acs.est.0c05356, 2020.

Wang, J., and Koel, B. E.: IRAS studies of NO_2, N_2O_3, and N_2O_4 adsorbed on Au (111) surfaces and reactions with coadsorbed H_2O, J. Phys. Chem. A, 102, 8573-8579, https://doi.org/10.1021/jp982061d, 1998.

Wang, J., and Koel, B. E.: Reactions of N_2O_4 with ice at low temperatures on the Au (111) surface, Surf. Sci., 436, 15-28, https://doi.org/10.1016/S0039-6028(99)00457-4, 1999.

Wexler, A. S., and Clegg, S. L.: Atmospheric aerosol models for systems including the ions H^+, NH_4^+, Na^+, SO_4^{2-}, NO_3^-, Cl^-, Br^-, and H_2O, J. Geophys. Res. Atmos., 107, ACH 14-11-ACH 14-14, https://doi.org/10.1029/2001JD000451, 2002.

Whalley, L. K., Furneaux, K. L., Goddard, A., Lee, J. D., Mahajan, A., Oetjen, H., Read, K. A., Kaaden, N., Carpenter, L. J., Lewis, A. C., Plane, J. M. C., Saltzman, E. S., Wiedensohler, A., and Heard, D. E.: The chemistry of OH and HO_2 radicals in the boundary layer over the tropical Atlantic Ocean, Atmos. Chem. Phys., 10, 1555-1576, https://doi.org/10.5194/acp-10-1555-2010, 2010.

Whalley, L. K., Stone, D., Dunmore, R., Hamilton, J., Hopkins, J. R., Lee, J. D., Lewis, A. C., Williams, P., Kleffmann, J., Laufs, S., Woodward-Massey, R., and Heard, D. E.: Understanding in situ ozone production in the summertime through radical observations and modelling studies during the Clean air for London project (ClearfLo), Atmos. Chem. Phys., 18, 2547-2571, https://doi.org/10.5194/acp-18-2547-2018, 2018.

Whalley, L. K., Slater, E. J., Woodward-Massey, R., Ye, C., Lee, J. D., Squires, F., Hopkins, J. R., Dunmore, R. E., Shaw, M., Hamilton, J. F., Lewis, A. C., Mehra, A., Worrall, S. D., Bacak, A., Bannan, T. J., Coe, H., Ouyang, B., Jones, R. L., Crilley, L. R., Kramer, L. J., Bloss, W. J., Vu, T., Kotthaus, S., Grimmond, S., Sun, Y., Xu, W., Yue, S., Ren, L., Acton, W. J. F., Hewitt, C. N., Wang, X., Fu, P., and Heard, D. E.: Evaluating the sensitivity of radical chemistry and ozone formation to ambient VOCs and NOx in Beijing, Atmos. Chem. Phys. Discuss., 2020, 1-41, https:\\doi.org\10.5194/acp-2020-785, 2020.

Winer, A. M., and Biermann, H. W.: Long pathlength differential optical absorption spectroscopy (DOAS) measurements of gaseous HONO, NO_2 and HCNO in the California South Coast Air Basin, Res. Chem. Intermed., 20, 423-445, https://doi.org/10.1163/156856794X00405, 1994.

1073 Wu, L., Li, X., and Ro, C.: Hygroscopic behavior of ammonium sulfate, ammonium nitrate,
1074 and their mixture particles, Asian J. Atmos. Environ., 13.3, 196-211,
1075 https://doi.org/10.5572/ajae.2019.13.3.196, 2019.

1076 Ye, C., Zhou, X., Pu, D., Stutz, J., Festa, J., Spolaor, M., Tsai, C., Cantrell, C., Mauldin, R. L.,
1077 Campos, T., Weinheimer, A., Hornbrook, R. S., Apel, E. C., Guenther, A., Kaser, L., Yuan,
1078 B., Karl, T., Haggerty, J., Hall, S., Ullmann, K., Smith, J. N., Ortega, J., and Knote, C.: Rapid
1079 cycling of reactive nitrogen in the marine boundary layer, Nature, 532, 489-491,
1080 https://doi.org/10.1038/nature17195, 2016.

1081 Ye, C., Heard, D. E., and Whalley, L. K.: Evaluation of novel routes for NO_x formation in
1082 remote regions. , Environmental Science Technology, 51, 7442-7449,
1083 https://doi.org/acs.est.6b06441, 2017a.

1084 Ye, C., Zhang, N., Gao, H., and Zhou, X.: Photolysis of particulate nitrate as a source of HONO
1085 and NO_x, Environ. Sci. Technol., 51, 6849-6856, https://doi.org/10.1021/acs.est.7b00387,
1086 2017b.

1087 Zhou, X., Gao, H., He, Y., Huang, G., Bertman, S. B., Civerolo, K., and Schwab, J.: Nitric acid
1088 photolysis on surfaces in low NO_x environments: Significant atmospheric implications,
1089 Geophys. Res. Lett., 30, 2217, https://doi.org/10.1029/2003GL018620, 2003.

1090

1091